Solubility of the Assemblage Pt-PtAs in Basalt with Implications for Pt-As Complexing and As Speciation

HBSc Undergraduate Thesis

By

Andrew C. Canali

Supervised by

Dr. James M. Brenan

Submitted April 11, 2014

Contents

1. Introduction

Investigation into the behaviour of platinum group elements (PGE- Os, Ir, Ru, Rh, Pt, and Pd) in magmatic systems allows for a deeper understanding of why exactly these elements behave the way they do when subjected to distinct parameters. Previous studies have noticed that the solubility of platinum (Pt), and other highly siderophile elements (HSE: Ni, Pd, Pt, Rh, Ir, Os) in silicate melts is affected when changing the temperature (T), pressure (P), oxygen fugacity (fO_2), and melt composition (M_x) (Borisov and Palme, 1995, 1997; Borisov et al, 1994; Capobianco et al, 1993; O'Neill et al., 2009; Ertel et al., 1999). That being said, there are limitations to understanding the mechanisms responsible for these relationships, for instance, under reducing conditions metallic contamination makes it difficult to viably quantify HSE content in melts due to widespread variation in analytical results. Since oxygen has been proven as a major complexing anion with Pt (e.g. Borisov and Palme, 1997), researchers have begun to question the affect of other complexing ligands. Recent research reveals the potential influence of sulfide bearing phases on the dissolution of PGE in silicate melts-for instance, attempting to define a relationship between sulfur fugacity (fS_2) influencing PGE solubility by complexing with S (Mungall and Brenan 2014; Fonsenca et al., 2009).

It may be reasonable to consider arsenic (As) as another complexing ligand with Pt, due to anomalous high grade PGE arsenide horizons in some magmatic ore deposits, which preferentially form as clusters in S-poor environments (e.g. Bushveld Complex-Maier, 1999). This phenomenon was investigated in more detail by Piña et al. (2013) and Hanley (2007); where the partitioning of siderophile and chalcophile (Sulfur loving) elements between arsenide phases, along with As-rich melts associated with high grade PGE ores are discussed respectively. The two localities from Hanley and Piña et al., exemplify the environments in which these deposits commonly occur – usually as mafic-ultramafic bodies hosting sulfide-arsenide PGE and polymetallic ore systems. Some of the main magmatic deposit types include: Kambalda type, which is a komatiite hosted deposit (e.g. Abitibi Greenstone Belt, Superior Province, Canada), and intrusive PGE mineralization (e.g. Voisey's Bay, Canada).

Since past research has yet to propose a direct relationship between arsenic (As) content in igneous systems and PGE solubility, it has sparked one's interest in attempting to develop a framework to help solve this geochemical problem. This study sets out to define the effects on the solubility of Pt, with the addition of As into mafic composition silicate melts (e.g. basalt) by means of high temperature experimentation (~1200°C) at an oxygen fugacity (fO_2) range of the fayalite-magnetite-quartz buffer(FMQ)+4 to ~FMQ – 3 ($\log fO_2$= -4.10 and -11.65). Through characterization of trace and major elements, using laser ablation-inductively coupled plasma-mass spectrometry (LA-ICP-MS) and electron microprobe analysis (EMPA) respectively, of As-bearing and As-free silicate glasses, one was able to note any significant changes in Pt solubility between the contrasting run-products. Very rarely is a pure arsenide phase suggested as a pathway for As-Pt complexing, since its interactions are usually studied symbiotically with sulfide in magmatic systems (e.g. Helmy et al., 2013; Piña et al., 2013). Hence, this study will provide further insight into PGE geochemistry, and the potential for Pt-As interactions in natural igneous systems.

1.1 PGE Behaviour in Silicate Melts

There are many previous studies that investigate the solubility of PGE in silicate melts, as well as the partitioning coefficients of these elements in variable magmatic systems to determine the dependence of PGE distribution with changes to *T, P,* fO_2 and M_x (e.g. Borisov et al., 1994; Borisov and Palme, 1993, 1997, 2000; Capobianco et al., 1993; Mungall and Brenan, 2014). Preliminary studies completed at the University of Toronto reveal a high partition coefficient for PGE to silicate melt, when considering partitioning from a sulfide melt, with D_{PGE}^{sul} values range from 2-3 X 10^6 (Mungall and Brenan, 2014) for Ir and Pt. Another significant finding was a notable increase in PGE solubility in S-bearing experiments. This increase in Pt solubility implies complexing of Pt with S in the melt. Nevertheless, the degree to which this group of elements is soluble in a given melt composition varies respectively. An example of this phenomenon is the comparison between the solubility's of palladium

(Pd) and Pt in the same diopside-anorthite (DA) eutectic at a log(fO_2) of -0.68, where up to 258 ppm of Pd (Borisov et al., 1994) and only 7.70 ppm of Pt is soluble at 1400°C (Borisov and Palme, 1997); therefore, indicating contrasting refractory properties. Since, in this study, temperature and pressure remain constant throughout experimentation the system is in turn mainly dependent on changes in fO_2. In comparison to other parameters, fO_2 seems to have the largest influence on enhancing PGE solubility through dissolution of a metal (Me) by reaction with O to form a metal oxide (MeO) in the silicate melt (Figure 1).

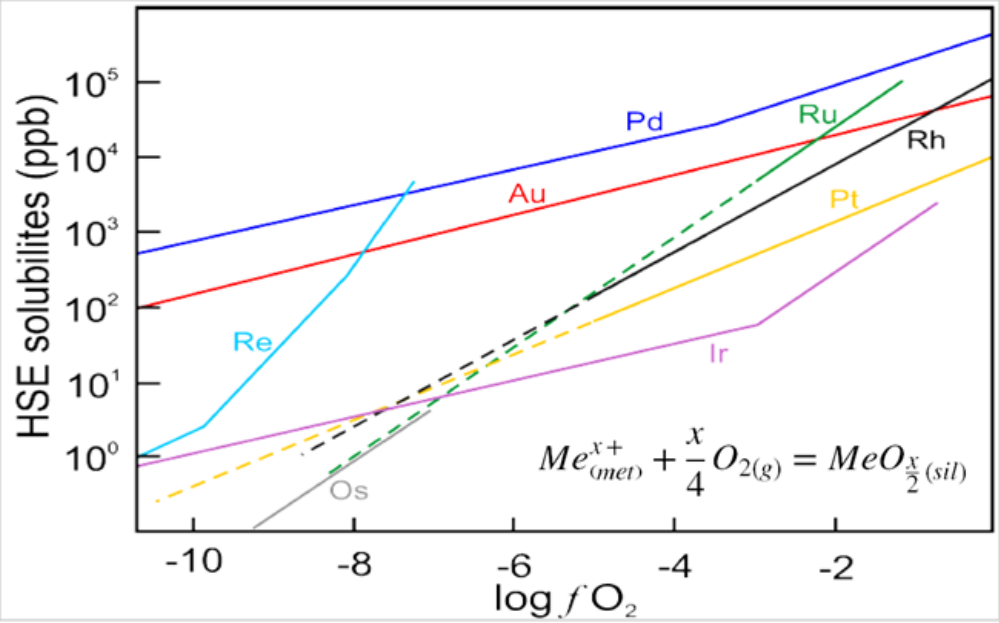

Figure 1: Summary of several investigations into HSE solubility in Fe-free silicate melts as function of fO_2 at 1300°C. The reaction in the bottom right is proposed as the main reaction controlling Pt solubility in silicate melts (see section 4.4 for details). Modified from Laurenz, 2012.

2. Experimental Methods

2.1 Overview and Starting Materials

The basis of my research consisted of a suite of high temperature experiments, which were all run at 1200°C in a bottom loading furnace at 1atm (See Figure 3 for materials). To avoid exposure to As in vapor phase, evacuated silica tubes were used to house the experiments. Within the silica ampoules was a solid oxide buffer mixture to fix the fO_2, along with a chromitite capsule made from a natural

cumulate in North Carolina, USA (Royal Ontario Museum reference #: M4557) which was used to contain the synthetic basaltic analogue combined with other desired constituents (e.g. Pt powder) (See Figure 4-method 1A for setup). High purity fused silica was used to construct the spacers necessary for separating the constituents in the experiment setup. The basaltic analogue (glass composition C-see Table 1) acted as the "silicate melt" basis for all experiments, and was synthesized by mixing high-purity oxides in a mortar and pestle under ethanol, then calcining overnight at 900°C, followed by fusion in an alumina crucible in air at 1 atm at 1400°C for 30 min.

Oxide	SiO_2	TiO_3	Al_2O_3	FeO	MgO	CaO*	Na_2O*	MnO_2	K_2O*	NiO	Total
wt% Oxide	46.90	5.41	8.80	15.41	9.18	12.04	1.54	0.21	0.51	0.20	100.20

Table 1: Oxide percents for glass composition C. Note, the asterisk indicates addition as carbonate.

The three buffers used to fix the fO_2 were: MnO-Mn_3O_4— $logfO_2$= -4.1, ΔFMQ= +4.3 (O'Neill and Pownceby, 1993); Ni-NiO— $logfO_2$= -7.72, ΔFMQ= +0.68 (O'Neill and Pownceby, 1993); Mo-MoO_2— $logfO_2$= -11.65, ΔFMQ= -3.3 (O'Neill,1986). Both the Mo-MoO_2 and Ni-NiO buffers were made by homogenizing 50:50 portions of the respective high purity metals and metal-oxides in a mortar and pestle under ethanol. On the other hand, MnO and Mn_3O_4 were both synthesized by sintering a portion of MnO_2 powder in a silica cup at specific conditions in a gas-mixing tube furnace according to O'Neill and Pownceby (1993). MnO was prepared by reducing MnO_2 at 1273K overnight ($CO:CO_2$=95:5), and Mn_3O_4 was formed by oxidizing MnO_2 at 1373K in pure CO_2 for 1 day. The metallic phases added to the capsule were: high purity Pt metal; and synthetic Pt+ PtAs eutectic formed according to the 1atm phase diagram (Figure 2). The synthesis of the Pt+PtAs melt was completed by combining the appropriate stoichiometric proportions of Pt and As in a silica tube, which was annealed at 500°C for 4 hours, then heated to 900°C for 1 day.

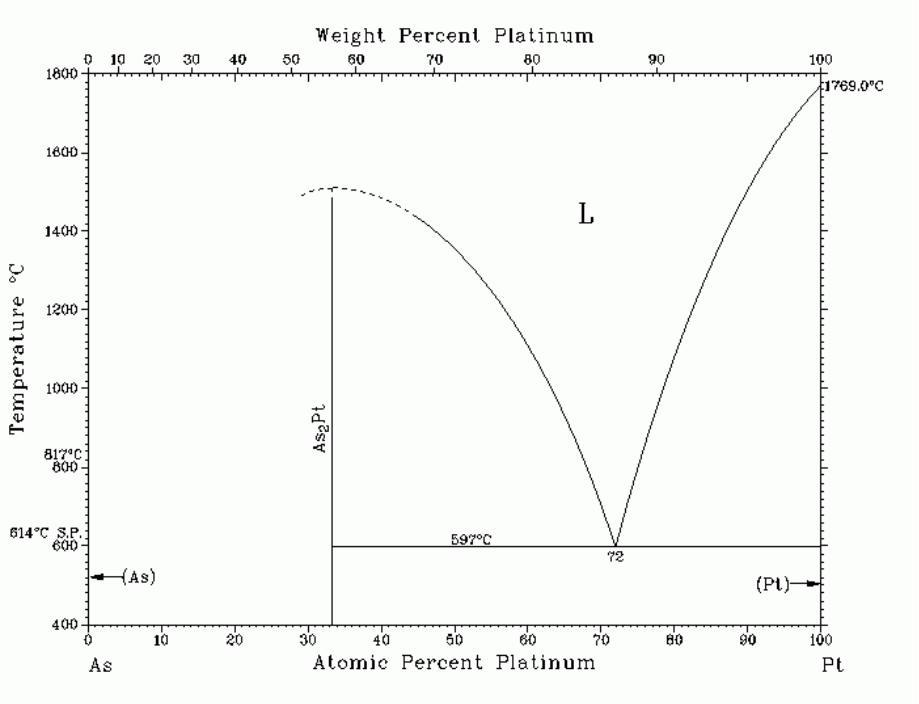

Figure 2: Arsenic-Platinum (As-Pt) phase diagram produced by Okamoto, 1990. This phase diagram provides the necessary conditions in order to synthesize the Pt+ PtAs eutectic (noted here at 72 at% Pt), which was used to fix the Pt and As activity in the melt.

A portion of crushed chromitite (~1wt%), was added into the mixture at a grain size <45µm, according to method 2, to ensure equilibration with surrounding melt during run duration. The Cr-spinel served as a proxy for estimation of fO_2 through vanadium (V) partitioning from Cr-spinel to silicate melt (Mallmann and O'Neill, 2009).

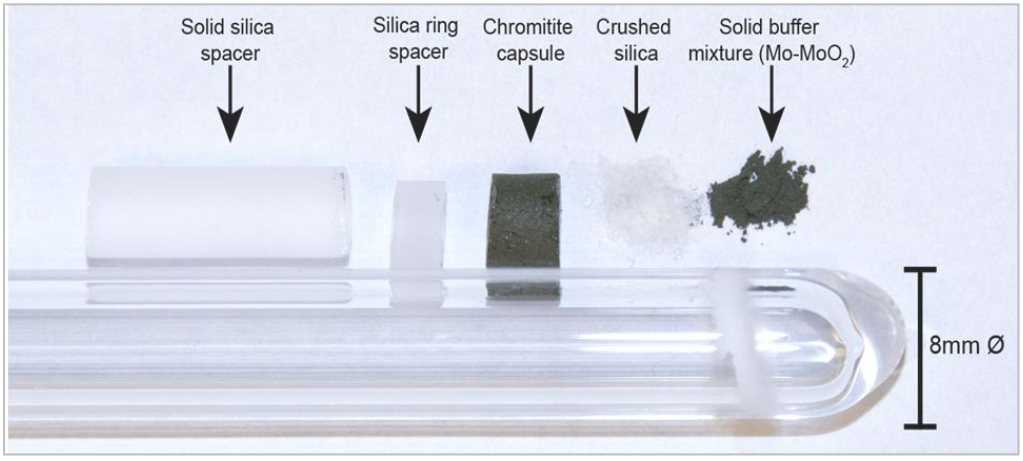

Figure 3: Photograph of starting materials. Each material is labelled by arrows, atop the silica tube in the appropriate order in which all the constituents would be inserted according to the layout in Figure 4.

2.2 Experimental Procedure

The procedure throughout one's research did not remain constant, since method 2 was proposed as an alternative after noticeable issues arose concerning loss of Pt and As during run duration using method 1. That being said, the general concept of experimentation did remain the same — where a silica tube (5mm I.D. X 8mm O.D.) sealed at one end was loaded with excess solid buffer at the bottom, followed by ground silica, on which the chromitite capsule filled with the specific components was placed, and then finally topped with a silica ring spacer and a solid silica spacer. This whole assembly was evacuated for ~1hr, then sealed using an oxy-acetylene torch and placed into an alumina cup, which served as the container during heating of the assembly in the bottom loader furnace. After the run duration had elapsed the experiments were placed into a salt+ice water solution, which was used in order to depress the freezing point of liquid water ensuring a more sudden quench. Experiments bearing an As component were all removed under a fume hood using appropriate personal protective equipment, and the oxide buffers were inspected using powder X-ray diffraction to ensure both phases were present after the run duration.

The three main setups (A, B and C) were split into two methods, noted in figure 4. The first of which shows the initial approach, where Pt+PtAs was added as the only means of Pt in the melt and then heated for a desired duration. The procedure for method 2 acted as a correction for the Pt and As stability issues, where the melt was first equilibrated with Pt powder (usually 4 days at 1200°C) at a given fO_2 to ensure Pt saturation, and then re-melted with the buffer removed for another 4 days with the Pt-PtAs melt to fix the As activity. Heterogeneity in the time resolved spectra produced by analysis with LA-ICP-MS of the most reducing run product glasses, suggests slow equilibration when subjecting the silicate glass fused in air to reducing conditions imposed by the buffers (Bennett and Brenan, 2013). One overcame this issue by re-fusing a new batch of starting material at FMQ-1 in a CO-CO_2 gas-mixing tube furnace at 1400°C, followed by thorough homogenizing in a mortar and pestle under

ethanol. Unfortunately, this was not done until much later in experimentation and the resulting run-products were unsuccessful.

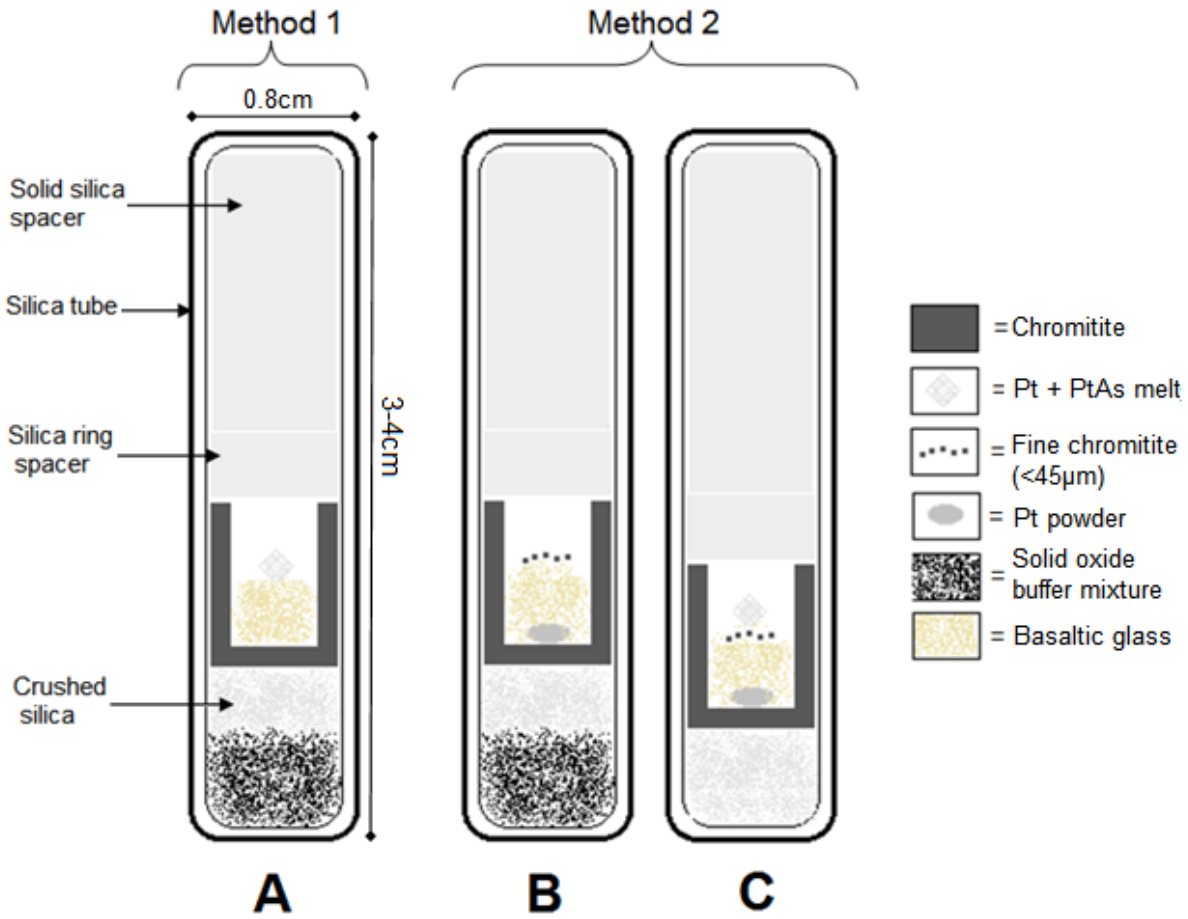

Figure 4: Schematic cross-section of experimental setup, distinguishing the two main methods used during experimentation. The above examples are fully sealed silica tube assemblies, following ~1 hour of vacuum evacuation, and are prepared for heating in the bottom loading furnace. In **method 1**, from bottom to top, sample **A** contains: a solid oxide buffer, crushed silica, a chromitite capsule filled with powdered basaltic glass, and a piece of the arsenide melt; topped with a silica ring spacer and a solid silica spacer to prevent heating of sample when sealing with the torch. For **method 2**, sample **B** differs from A in that, Pt powder was added excluding the As phase, and after an initial run it was then resealed and melted with the Pt-PtAs with no buffer, yielding sample **C**. For the purpose of convenience method 2-B and C, shows the presence of fine chromitite.

3. Analysis of Run-Products

All run-products were mounted in an epoxy puck and grinded into using silicon carbide paper until the experiments were adequately exposed, and a final polishing was completed using 1 and 0.3µm alumina. A Cameca SX50 electron microprobe at the University of Toronto was used for major element analysis. Resulting silicate glasses were analyzed using a 15kV accelerating voltage and a 10nA beam

current at a defocused beam width of 10µm. Alloy phases were analyzed using a 10µm beam as well, at an accelerating voltage of 20kV with a 30na beam current. Standards used for silicate glass analysis included: natural basalt glass-Si, Fe, Al, Mg, Ca; bustamite-Ca; albite-Na; barite-Ba. High purity metals were used as standards during alloy analysis.

LA-ICP-MS at the University of Toronto was used to determine the trace element composition of the silicate glasses. Samples were ablated using a frequency quintupled Nd-doped Yttrium aluminum-garnet (YAG) laser, which was paired with a VG PQExcell quadrupole mass spectrometer. The detector consisted of a photomultiplier tube, which was able to switch between pulse counting and analog depending on count rate (counts per second-cps); during analysis of one's experiments counts never exceeded 2,000,000cps, so the detector remained in analog mode. Ablation of the glass was done at a frequency of 10Hz, with spot analysis ranging from 50-100 µm. The spot size was reduced when analyzing the Cr-spinel (fine chromitite) grains present in the glass, where an 8-12 µm spot was unitized at a frequency of 4Hz. During the 80 s data acquisition period for each analysis, 20 s of "background" was obtained, prior to the 60s acquisition of ablated material. There was a 60 s washout period in between each analysis. Pre-ablation of the area of interest and flushing with He allowed for the removal of any surface impurities, providing a more reliable result during data acquisition. NIST610 was used as the standard glass during analyses, which was analyzed prior to, and after a block of no more than 15 analyses. Data reduction was completed using the GLITTER software package, version 4.4. The trace element concentration of the NIST610 standard glass was used during data reduction, which contains 3.12ppm Pt and 35.7ppm As (Jochum et al., 2011). Calcium was used as the internal reference element to deduce ablation yields from the silicate glass. Table 2 provides a summary of the major and trace element analysis of the silicate glasses and alloy phases.

		Sp1	1σ	Sp2	1σ	Sp4	1σ	Sp5	1σ	Sp7	1σ	Sp8	1σ	Sp9	1σ
Parameters	T(°C)	1200		1200		1202		1202		1202		1203		1203	
	Buffer	Ni-NiO		Mo-MoO2		Mo-MoO2		Ni-NiO		MnO-Mn3O4		Ni-NiO		Ni-NiO	
	log fO_2	-7.72		-11.65		-11.65		-7.72		-4.10		-7.72		-7.72	
	ΔFMQ	0.68		-3.25		-3.25		0.68		4.30		0.68		0.68	
	duration (hrs)	69.50		65		87.33		87.33		87.33		23.50		47.66	
	glass comp	C		C		C		C		C		C		C	
Silicate (wt%)	SiO2	46.68	0.37	47.02	0.24	51.93	0.31	47.88	0.36	47.74	0.58	47.21	0.35	47.37	0.49
	TiO2	5.18	0.28	5.17	0.15	5.81	0.24	5.17	0.16	5.71	1.57	5.36	0.24	5.12	0.16
	Al2O3	15.55	0.13	16.03	0.13	15.66	0.20	15.79	0.16	16.08	4.75	15.85	0.12	15.92	0.14
	FeO	11.10	0.12	8.90	0.09	3.51	0.31	9.05	0.24	8.66	2.01	9.68	0.28	9.32	0.19
	MgO	8.17	0.13	8.39	0.09	8.88	0.15	8.66	0.09	5.12	1.34	8.45	0.10	8.23	0.16
	CaO	11.76	0.16	12.24	0.12	12.57	0.14	11.72	0.14	11.68	1.76	11.55	0.11	11.90	0.13
	Na2O	0.71	0.05	0.73	0.05	0.62	0.04	0.41	0.03	0.59	0.08	0.57	0.04	0.67	0.05
	MnO	0.17	0.07	0.19	0.05	0.19	0.04	0.17	0.04	0.10	0.04	0.16	0.05	0.17	0.03
	K2O	0.18	0.03	0.17	0.02	0.19	0.02	0.10	0.02	0.22	0.05	0.18	0.03	0.18	0.02
	Oxide Totals	99.57	0.60	99.03	0.34	99.63	0.36	99.01	0.67	95.99	1.53	99.06	0.37	98.98	0.78
	ppm As	330.04	35.02	16.92	10.89	15.54	5.49	238.82	48.79	14684.32	1681.41	437.87	48.13	416.58	50.41
	ppm Pt	0.048	0.010	0.034	0.007	0.018	0.007	0.010	0.005	0.171	0.035	0.090	0.003	0.077	0.015
Alloy (at%)	Fe	7.31		19.65		15.18		6.95		1.17		6.78		6.73	
	Pt	91.23		74.86		83.60		92.65		97.93		91.63		91.97	
	aPt alloy	0.51		0.08		0.17		0.54		0.95		0.55		0.55	
[3][Pt] = 1	ppm Pt	0.094	0.019	0.405	0.083	0.103	0.040	0.018	0.009	0.181	0.037	0.165	0.005	0.139	0.027

Table 2: Summary of phase compositions and respective Pt solubilities in run product glasses. Note: [1]= Experiment initially run for 87.3 hours at Ni-NiO buffer (1202° C), then re-equilibrated at Mo-MoO2 buffer for 91 hours (1203° C), [2]= As-free experiments, and [3]= Value corrected to unit activity of Pt calculated from the Pt content of the metal phase.

		[1]Sp10	1σ	[2]Sp11	1σ	[2]Sp12	1σ	[2]Sp13	1σ	Sp14	1σ	Sp15	1σ
Parameters	T(°C)	1203		1202		1202		1202		1202		1202	
	Buffer	Ni-NiO/Mo-MoO2		Ni-NiO		Mo-MoO2		MnO-Mn3O4		MnO-Mn3O4		Mo-MoO2	
	log fO_2	-11.65		-7.72		-11.65		-4.10		-4.10		-11.65	
	ΔFMQ	-3.25		0.68		-3.25		4.30		4.30		-3.25	
	duration (hrs)	91.00		94.50		94.50		94.50		48		45.50	
	glass comp	C		C		C		C		C		C	
Silicate (wt%)	SiO2	49.98	0.26	46.18	0.37	48.47	0.34	48.48	0.52	46.25	0.35	46.90	0.24
	TiO2	5.61	0.3	5.19	0.21	4.93	0.18	5.92	0.32	5.24	0.26	5.16	0.26
	Al2O3	15.20	0.17	15.54	0.18	15.23	0.12	14.96	1.12	15.38	0.17	16.11	0.11
	FeO	6.87	0.18	11.60	0.24	10.33	0.21	11.13	0.66	10.47	0.22	9.09	0.21
	MgO	8.80	0.11	8.44	0.11	7.89	0.11	6.76	0.42	6.83	0.12	7.99	0.11
	CaO	11.91	0.1	11.35	0.14	11.31	0.09	11.46	0.40	10.99	0.11	12.04	0.20
	Na2O	0.37	0.04	0.56	0.05	0.86	0.05	0.55	0.05	0.52	0.05	0.94	0.05
	MnO	0.15	0.04	0.17	0.04	0.18	0.05	0.15	0.04	0.15	0.05	0.16	0.05
	K2O	0.07	0.02	0.17	0.02	0.25	0.03	0.20	0.03	0.17	0.03	0.22	0.02
	Oxide Totals	99.27	0.54	99.19	0.61	99.45	0.62	99.61	0.48	96.01	0.55	98.60	0.57
	ppm As	8.32	3.62	nd		nd		nd		10384.97	504.07	10.57	3.99
	ppm Pt	0.004	0.003	0.011	0.005	0.053	0.012	0.133	0.028	0.188	0.044	0.078	0.025
Alloy (at%)	Fe	16.09		7.00		18.27		1.19		1.34		19.66	
	Pt	83.53		91.48		76.64		98.23		97.58		76.42	
	aPt alloy	0.16		0.53		0.11		0.94		0.93		0.09	
[3][Pt] = 1	ppm Pt	0.025	0.019	0.021	0.009	0.500	0.113	0.141	0.030	0.201	0.047	0.876	0.281

Table 2 continued.

4. Results

4.1 Run Product Textures

The resulting run products all displayed similar textural relationships; where the quenched basaltic glass exhibited a wetting meniscus clinging to each side of the chromitite capsule, with a metallic phase (e.g. Pt-Fe alloy) present as a bead either at the bottom or top of the glass (See Figure 5). Blebs of the Pt-arsenide melt were usually suspended at the top of the meniscus, due to its tendency to pool at the melt-air interface. For the most part the silicate glasses lacked any crystal phase, aside from the crystallization of Ca-rich plagioclase, as determined by the energy dispersive spectrometer (EDS) equipped to the scanning electron microscope (SEM) at the University of Toronto. Along with the plagioclase, chromium-spinel (Cr-spinel) sometimes crystallized out of the melt, which is most likely due to the high concentrations of dissolved Cr; however, both the plagioclase and spinel were easily avoided during analysis. Pore spaces (20-100µm) were often preserved in the glass, which indicates the entrapment of a gaseous phase upon quenching.

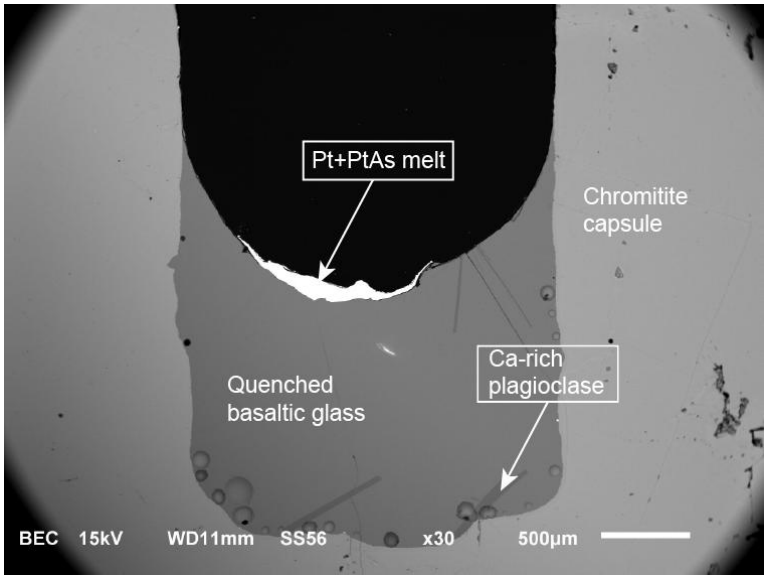

Figure 5: Backscattered electron image (BSEI) of the typical run product (SP2) textures, produced using the JEOL JSM-6610LV SEM. Contained in the chromitite capsule is a bright immiscible metallic phase (Pt+PtAs melt) atop quenched basaltic glass with laths of Ca-rich plagioclase radiating from the base of the capsule and the glass meniscus. Small pores are seen along chromitite-glass interface.

The Pt+PtAs eutectic used in the experiments consisted of a two-phase assemblage, where solid Pt metal nuggets were suspended within a dendritic PtAs melt (See Figure 6).

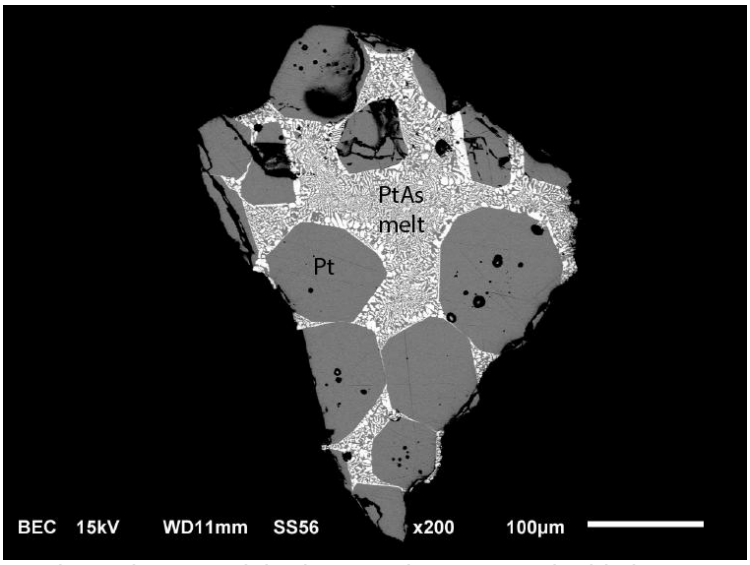

Figure 6: BSEI of Pt+PtAs melt starting material. The two phases seen in this image are Pt suspended in a PtAs melt.

4.2 Run-Product Homogeneity

In order to assess the homogeneity of the run product glasses, the method proposed by Bennett and Breanan (2013) was used, where the ratio of the respective time resolved spectra (TRS) provided from LA-ICPMS analyses of the siderophile element in question and a stable lithophile element in the melt was plotted against time; in this case it was $^{195}Pt/^{43}Ca$ vs. Time (s) (Figure 7-1 and 2)**.** This method revealed the samples containing Pt micro-inclusions by highlighting anomalous changes in the signal aside from the inherent fluctuations, such as those produced by ablation and plasma instability, which should be ubiquitous to both the Pt and Ca assuming the glass is homogenous. The main inference from the plots suggests the glasses became progressively more heterogeneous with respect to Pt solubility as fO_2 decreased, implying that the formation of Pt micronuggets was not fully avoided. The box plots in Figure 7 are both chosen from a section of TRS ~20sec into ablation and clearly display the differences between the degree of scatter for the low (Mo-MoO_2 buffered) and high fO_2 (MnO-Mn_3O_4) runs- SP4 and SP7 respectively. It is also important to note that an average of 4 spots were analyzed on each glass from top (near the meniscus) to bottom (near the capsule-melt boundary), so the runs plotted in Figure 7 represent the TRS produced from top and bottom of the experiments, and should help identify any gradient present in the glass. Although the highest fO_2 run at the MnO-

Mn_3O_4 buffer (FMQ+4.3) did display the lowest standard deviation with respect to the mean (s= 2.04E-4 and x̄= 5.01E-4 — SP7 Spot#1), this trend changed dramatically with the fO_2 change to FMQ+0.68 using the Ni-NiO oxide buffer, and even more so when under most reducing conditions at FMQ-3.25 (s= 2.27E-3 and x̄= 2.34E-4 — SP4 Spot#2) (Table 3). In turn, there is a certain degree of ambiguity when selecting integration of "stable" areas of ablation, so the statistical interpretation may be used as a guideline when selecting the appropriate sections. Stable areas were considered to be the lowest count rate, for 15-20s; however, in some cases the area selected was much smaller due to erratic variation in the TRS. Figure 8 shows the typical change in signal when encountering Pt nuggets in the glass, and the area considered for integration.

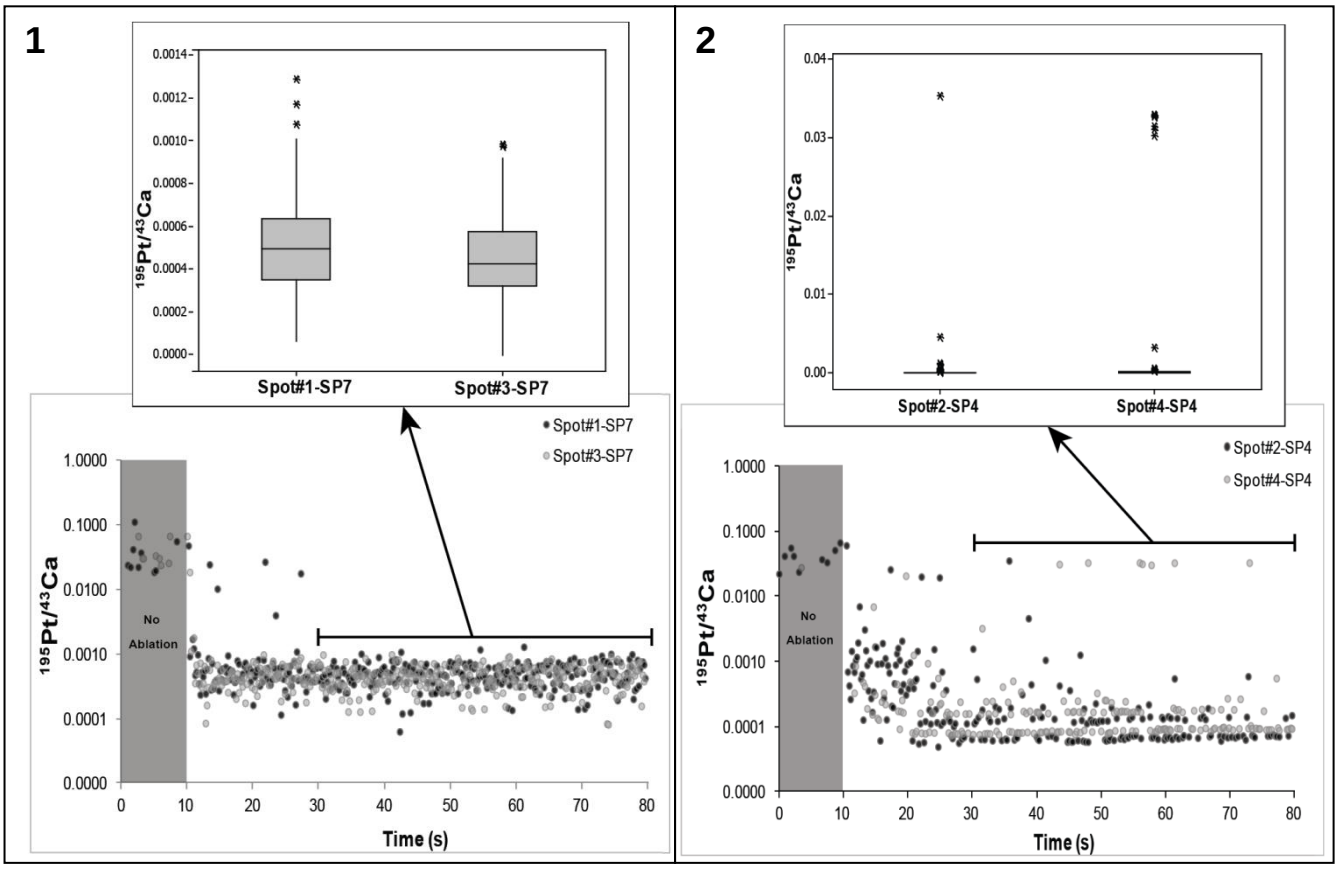

Figure 7: Time resolved spectra from LA-ICPMS analysis ratio plots of $^{195}Pt/^{43}Ca$ and respective box plots for the selected ranges as outlined by the capped black line with an arrow. **1** (left) represents the TRS for oxidizing runs at the MnO-Mn_3O_4 buffer (SP7), which displays a tight spread with few outliers as depicted by the respective box plot with a normal distribution– allowing for viable interpretation when constraining Pt solubility. **2** (right) displays the TRS resulting from analysis of the reducing runs at the Mo-MoO_2 buffer. The increase in scatter is expressed well in the resulting box plot having a noticeable right skew, indicating there is extensive metal contamination by micro nuggets of Pt; hence, the reducing runs were not used to constrain Pt solubility due to inconsistency in results. See table 3 for accompanying summary statistics.

(^{195}Pt/ ^{43}Ca) Spot- SP7		(^{195}Pt/ ^{43}Ca) Spot 3-SP7		(^{195}Pt/ ^{43}Ca) Spot 2- SP4		(^{195}Pt/ ^{43}Ca) Spot 4- SP4	
Mean ($\bar{x}$)	5.01E-04	Mean ($\bar{x}$)	4.51E-04	Mean ($\bar{x}$)	2.34E-04	Mean ($\bar{x}$)	9.99E-04
Standard Deviation (s)	2.04E-04	Standard Deviation (s)	1.87E-04	Standard Deviation (s)	2.27E-03	Standard Deviation (s)	5.33E-03
Standard Error ($SE_{\bar{x}}$)	1.30E-05	Standard Error ($SE_{\bar{x}}$)	1.19E-05	Standard Error ($SE_{\bar{x}}$)	1.45E-04	Standard Error ($SE_{\bar{x}}$)	3.40E-04
Median	4.96E-04	Median	4.25E-04	Median	6.19E-05	Median	8.27E-05
Mode	3.22E-04	Mode	5.17E-04	Mode	0	Mode	0
Skewness	0.551	Skewness	0.411	Skewness	15.25	Skewness	5.70
Range	1.23E-03	Range	9.83E-04	Range	0.035	Range	0.033
Minimum	6.316E-05	Minimum	0	Minimum	0	Minimum	0
Maximum	1.29E-03	Maximum	9.83E-04	Maximum	0.035	Maximum	0.033
Sum	0.124	Sum	0.111	Sum	0.058	Sum	0.246
Count	247	Count	247	Count	246	Count	246

Table 3: Summary statistics for the range outlined by the capped black lines above the TRS in Figure 7.

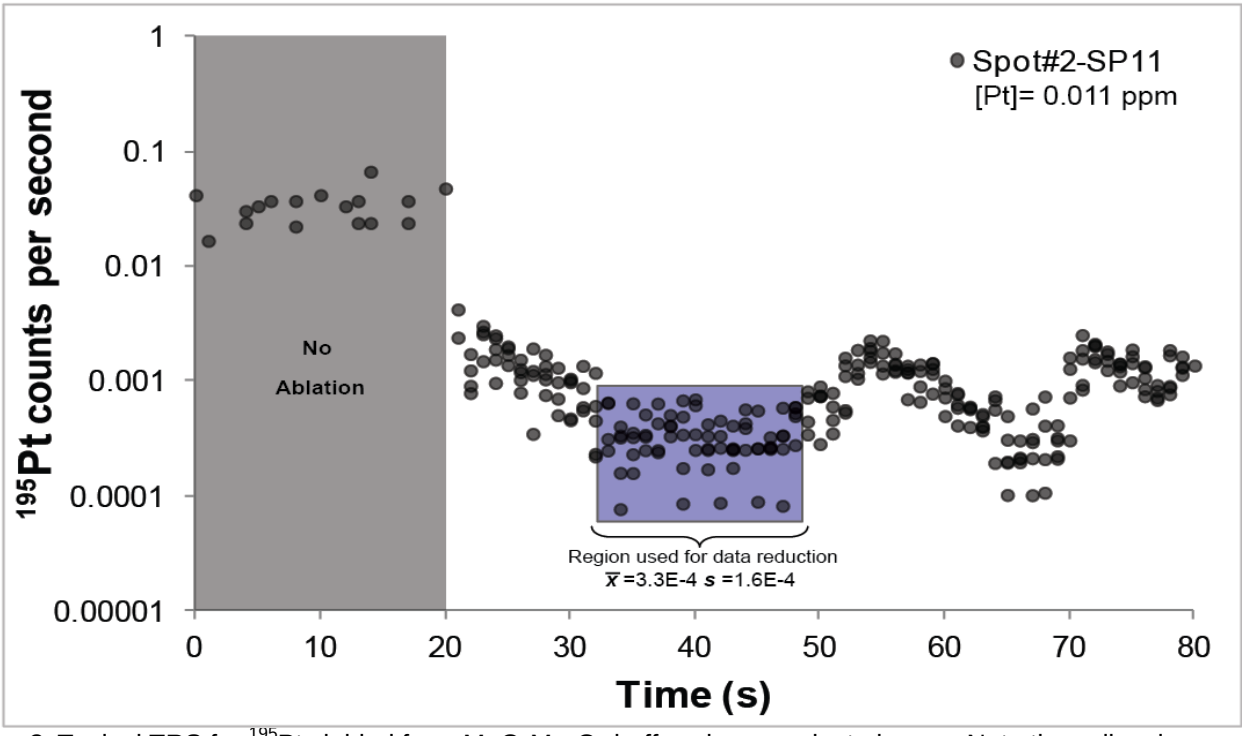

Figure 8: Typical TRS for ^{195}Pt yielded from MnO-Mn_3O_4 buffered run product glasses. Note the spikes in counts between 50 to 80sec, and the blue shaded area considered for integration during data reduction. The calculated sample standard deviation (s) is 1.6 E-4 cps and sample mean ($\bar{x}$) is 3.3E-4 cps for the area selected for integration.

4.3 Time and fO_2 Dependence Of Pt and As Content in Run-Product Glasses

In order to assess equilibration of the run-product glasses, a time series was completed, where each experiments at a fixed fO_2 was run for different durations within a 4 day period. Results of the time series indicate that the solubility of both Pt and As in the glasses is time dependent. This was indicated by a distinct incremental loss of As with time in the Ni-NiO buffered runs, varying from 437.87±48.13 ppm to 238.82±48.79 ppm As at 24 and 87 hours respectively (Figure 9). In fact, the runs at Ni-NiO displayed many of the trends best regarding time and fO_2 dependence of both Pt and As content in the melts, therefore, they were used for most of the interpretation.

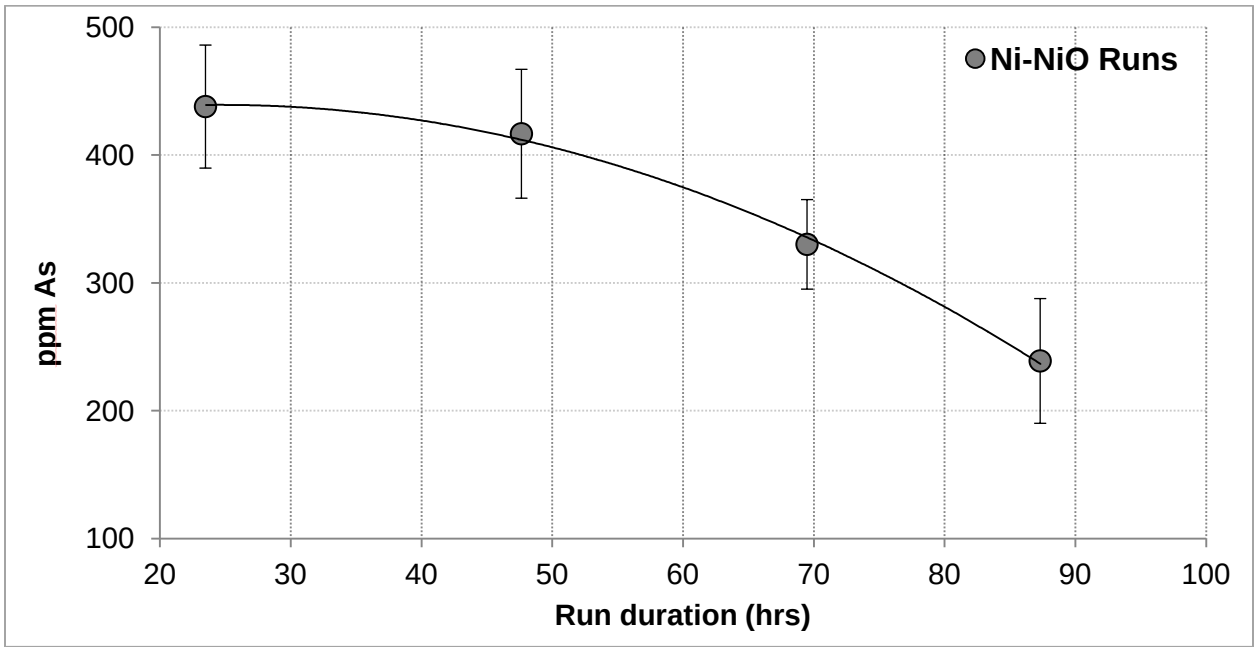

Figure 9: Plot of As solubility and run duration; exhibiting a clear negative correlation between the two variables, indicating a decrease in As content with increasing run duration. Error bars express one standard deviation.

The loss of As may be explained by a reaction between As in vapor phase ($As_{2(g)}$) with the buffer at the bottom of the silica ampoule ($Ni_{(s\text{-}buffer)}$):

$$Ni_{(s-buffer)} + \frac{1}{2} As_{2(g)} = NiAs_{(s-buffer)} \qquad (1)$$

The proposed interaction was confirmed by EDS of the buffer to contain both NiO and NiAs (Figure 10). This phenomenon was the main reason for implementing the method 2, as mentioned above, where the

arsenide melt was added to experiments following equilibration at a given fO_2 and re-melted to eliminate the possibility of losing As to the buffer.

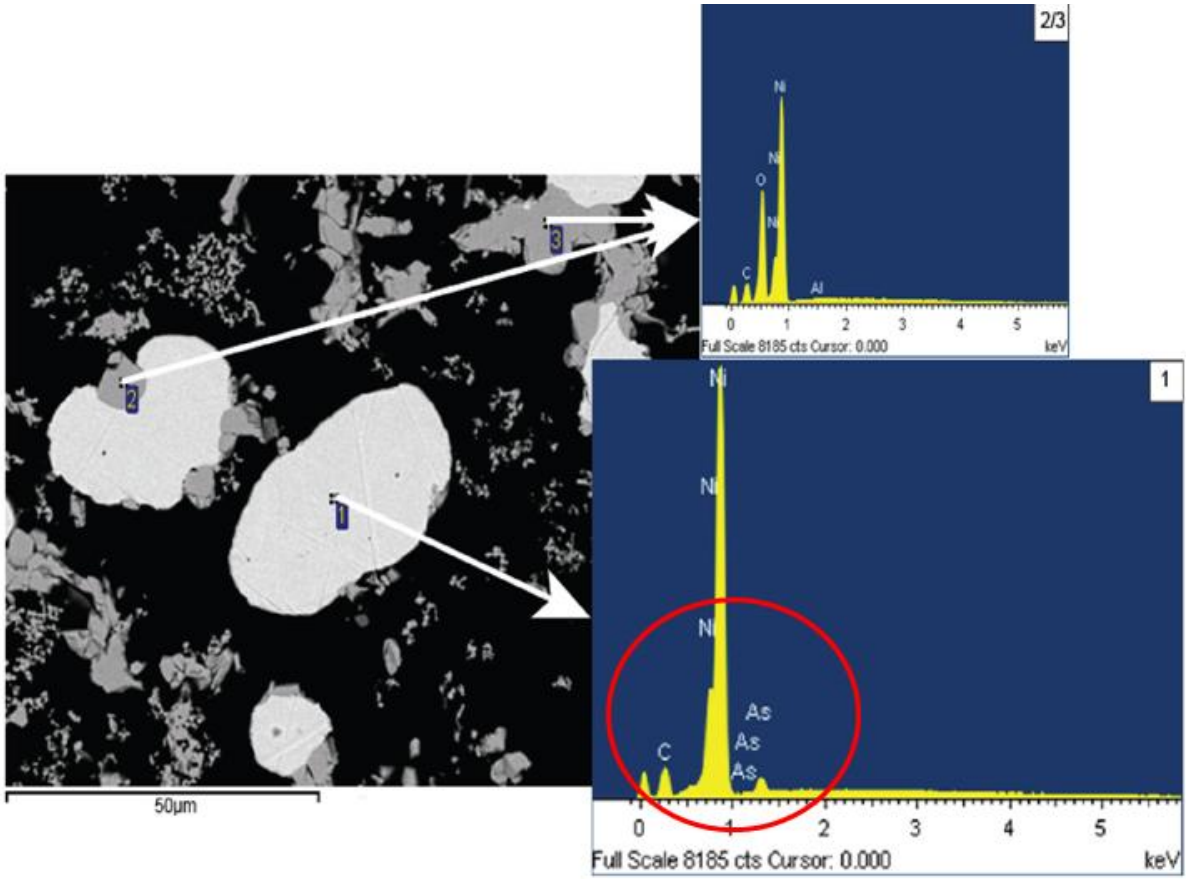

Figure 10: BSEI of the Ni-NiO buffer mixture, where NiO is the darker grey phase and Ni is represented by the brighter phase. Note that the EDS indicated the presence of As in the Ni, as highlighted by the red circle on spectrum 1.

However, due to the lack of the PtAs melt in the majority of the Mo-MoO_2 and MnO-Mn_3O_4 run product alloys it is difficult to accurately model the relationship between As content and time, since there may have been a greater solubility resulting in the run products with more PtAs melt added prior to the run. The gradient revealed by the top to bottom spot analysis using LA-ICPMS supports the loss of As from the glasses, which would be expected if a component were not in equilibrium with the silicate phase. The instability of As in the run-product glasses was most apparent in the reducing runs (Mo-MoO_2) with 8ppm near the melt meniscus, and 31ppm near the melt-capsule boundary at the bottom for experiment SP2 (Figure 11).

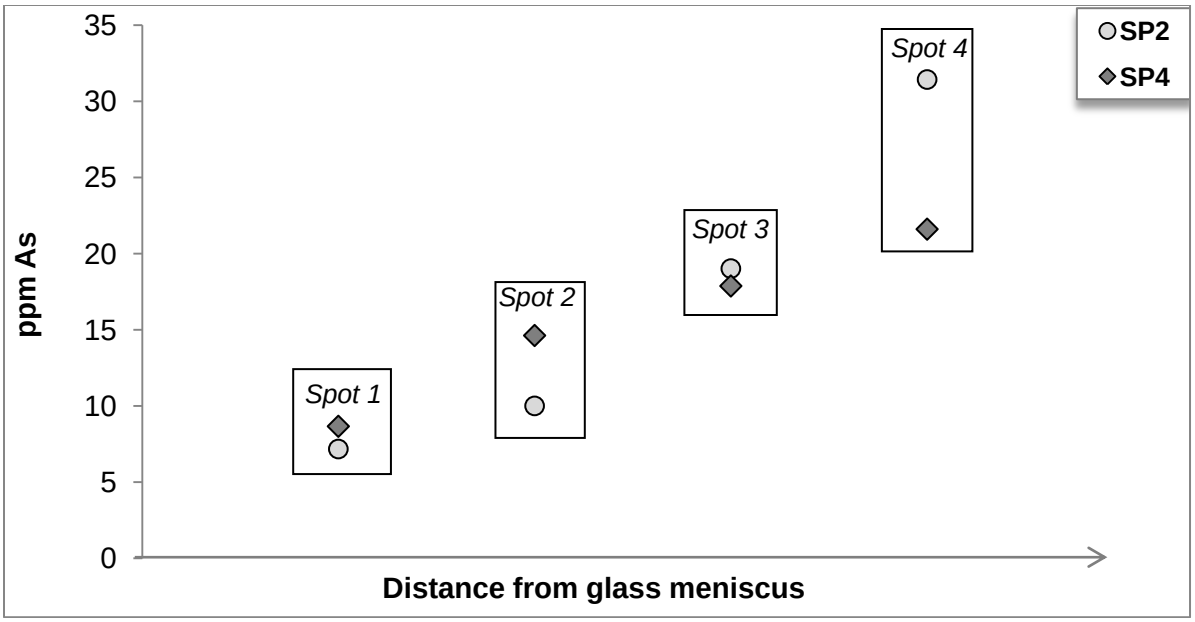

Figure 11: Plot of As concentrations yielded from a top to bottom LA-ICPMS spot analysis progression. It was apparent that As is volatilizing from the melt the most from runs under reducing conditions. Both SP2 and SP4, seen here, were run at the Mo-MoO_2 buffer ($logfO_2$= -11.65).

Regarding Pt content, a decrease in solubility was apparent with increasing run duration, which seems to be associated to the decrease in As content, assuming that Pt complexing with an arsenic component is plausible. This potential relationship is exhibited most clearly for the Ni-NiO runs, where there is a ubiquitous decrease in As and Pt content with increasing run duration (Figure 12). There is also a loss of Pt with time in the more reduced and oxidized runs, which does not directly correspond to the respective As content in each of the glasses. However, there are factors which explain this phenomenon: (1) the extremely reducing conditions for the Mo-MoO_2 buffered experiments yield no stable Pt concentrations due to the excessive scatter, so the variation in Pt content would occur regardless of time due to the influence of micro-nuggets forming at such reducing conditions; and (2) the more oxidizing MnO-Mn_3O_4 runs exhibit a greater dependence on oxygen with a negligible increase in Pt solubility with increasing As content, implying the majority of Pt complexes with oxygen, so dramatic increase or decrease in As content would have little influence on the Pt content under more oxidizing conditions.

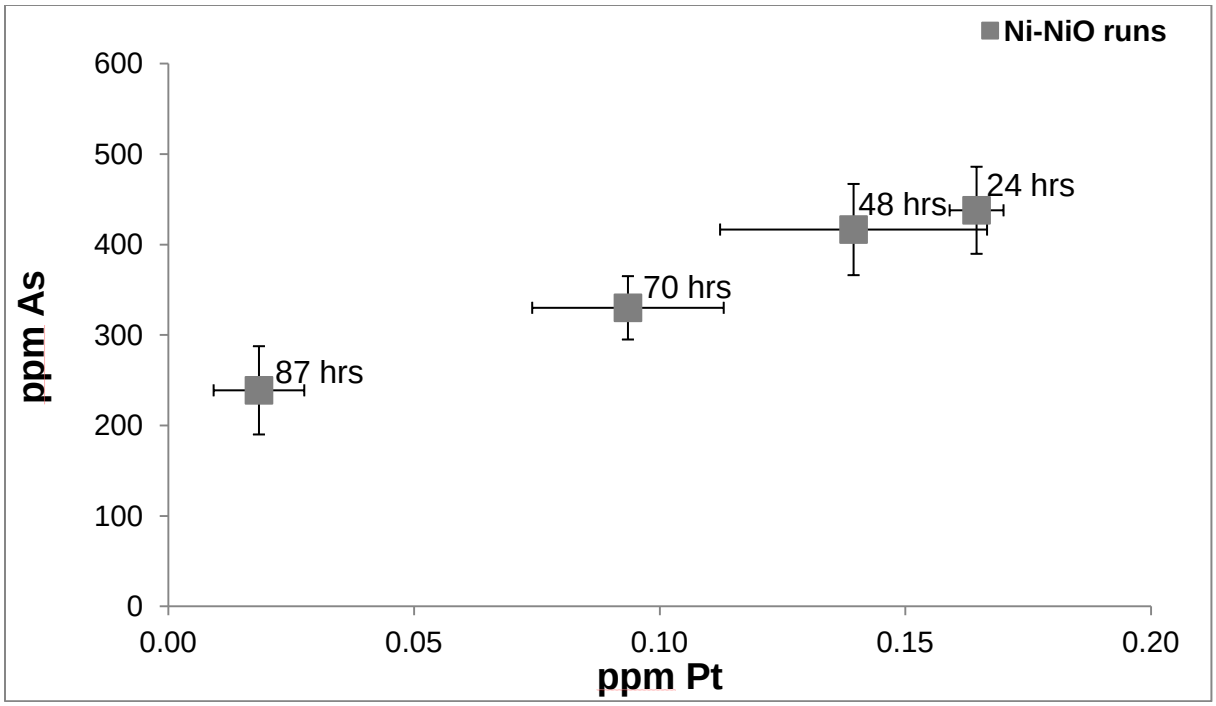

Figure 12: Plot of As solubility and Pt solubility at different run durations for experiments run with the Ni-NiO buffer. There is a noticeable loss of both Pt and As with increasing run duration, which implies a dependence of both components on one-another in the melt.

Changes in fO_2 yielded the most significant influence on Pt content, which was expected considering the extensive research already completed regarding the affect of fO_2 on PGE solubility. Generally there was a direct positive correlation between Pt content and fO_2, where an increase in fO_2 resulted in a greater Pt solubility. This relationship indicates the tendency for platinum to exist as an oxide species in the melt.

The same trend was noticed for As, where an increase in solubility was directly associated with an increase in fO_2 (Figure 13), which indicates the presence of As-oxide species in the melt. At the lowest fO_2 ($\log fO_2$= -11.65) ~10 ppm of As was soluble, where at the highest fO_2 ($\log fO_2$= -4.10) the solubility increased dramatically to up to nearly 1.5 wt%. Since no PtAs was detected in the MnO-Mn_3O_4 buffered run product alloys, it implies the runs were not saturated in the PtAs melt; however, method 2 run products maintained arsenide saturation and yielded a similar As solubility.

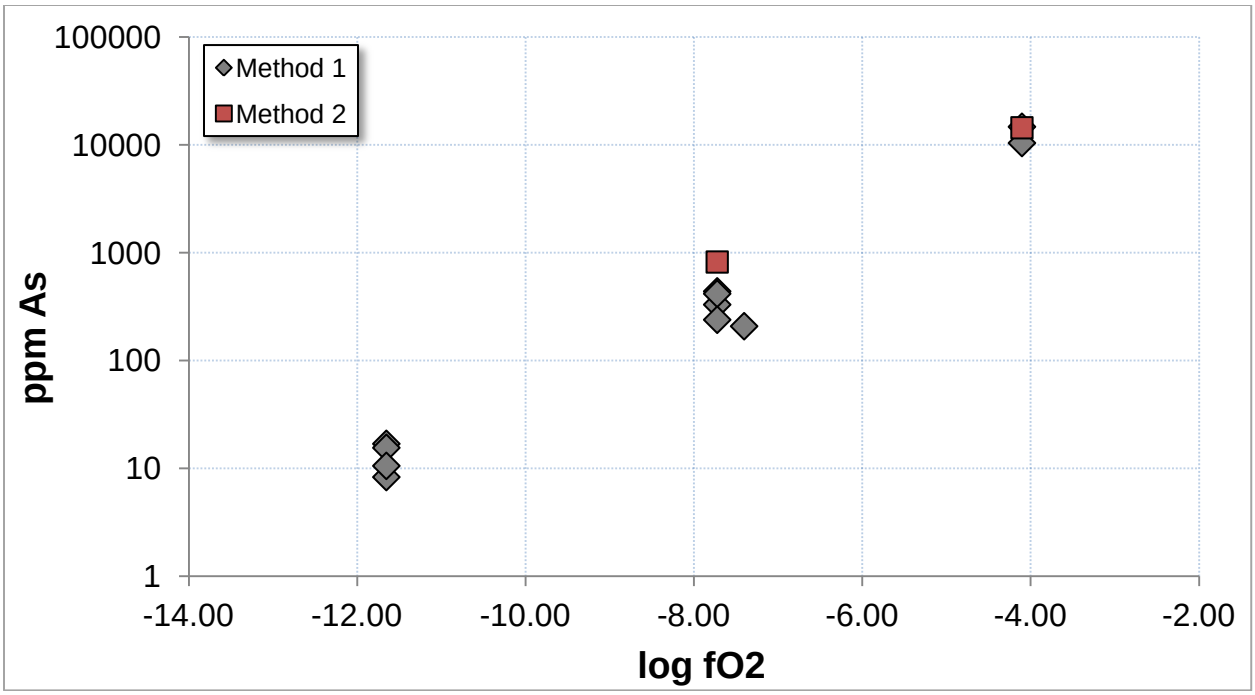

Figure 13: As solubility as a function of log(fO_2). The plot implies a direct dependence of As solubility of fO_2, with values ranging from ~10ppm at reducing conditions ($logfO_2$=-11.65) to ~10000ppm at oxidizing conditions ($logfO_2$= -4.10). This dramatic change in solubility over the fO_2 range suggests changes in As oxidation state in the melt.

4.3.1 Method 2 Experiments: Limiting As Loss with Time

As previously mentioned, method 2 was proposed as a means to limit the reaction between As and the buffer at the base of the experiment (e.g. equation 1) during run duration, and it was employed for experiments M2-Sp3 to M2-Sp6 (Table 4).This was only necessary for the Ni-NiO runs, since it was the only buffer that reacted with the As; this is likely due to the uncoupled Ni being more reactive in contrast to the stable oxides (e.g. NiO, MnO). The As content of the glass from M2-Sp4, which was pre-equilibrated at a $logfO_2$ of -7.72 for 4 days and re-melted without the buffer with the addition of the Pt-PtAs , was 819.51 ±6.60 ppm which is nearly double that of even the highest concentration of the method 1 runs (Figure 15). This implies that As-Ni interactions induced by the buffer accounts for a significant loss of As from the glass.

		[1]M2-Sp3	1σ	[2]M2-Sp4	1σ	[1]M2-Sp5	1σ	[2]M2-Sp6	1σ
	T(°C)	1200		1200		1200		1200	
	Buffer	Ni-NiO		Ni-NiO		MnO-Mn3O4		MnO-Mn3O4	
	log fO_2	-7.72		-7.72		-4.10		-4.10	
	ΔFMQ	0.68		0.68		4.30		4.30	
	duration (hrs)	96		192		96		192	
	glass comp	C		C		C		C	
silicate (wt%)	SiO2	47.71	0.12	47.52	0.21	50.69	0.40	49.58	0.40
	TiO2	5.28	0.17	5.00	0.19	6.04	0.18	5.74	0.23
	Al2O3	15.27	0.06	15.02	0.11	14.38	0.09	14.64	0.13
	FeO	10.88	0.11	11.58	0.19	9.37	0.19	9.19	0.15
	MgO	8.82	0.10	8.79	0.09	5.88	0.07	6.03	0.07
	CaO	12.06	0.17	11.86	0.15	11.90	0.16	12.03	0.05
	Na2O	0.48	0.03	0.44	0.06	0.44	0.04	0.91	0.06
	MnO	0.19	0.03	0.19	0.04	0.11	0.03	0.12	0.03
	K2O	0.12	0.02	0.08	0.02	0.16	0.03	0.14	0.04
	Oxide Totals	100.82	0.33	100.47	0.41	98.96	0.64	98.38	0.75
	ppm As	nd		819.51	6.60	nd		14376.92	804.45
alloy at%	Fe	7.44		-		1.24		-	
	Pt	91.02		-		97.09		-	
	aPt alloy	0.506				0.942			
[3][Pt] = 1	ppm Pt	0.036	0.004			0.064	0.021		

Table 4: Summary of phase compositions from method 2 run product glasses. Note: 1= As-free experiments, 2= As bearing experiments and 3= Value corrected to unit activity of Pt calculated from the Pt content of the metal phase.

Unfortunately, the Pt content of the glasses bearing an arsenide phase, such as M2-Sp4, was not accurate with relation to initial experiments. This is due to the extremely low [Pt] in the melt, reflected by the once Pt-Fe saturated precursor run product for M2-Sp4 which contained only Pt-As alloy after the re-melt in the presence of the arsenide phase; usually both alloy phases are present, and the lack of Pt-Fe indicates undersaturation of Pt. The Pt-PtAs starting material was re-synthesized prior to completion of the method 2 experiments and compositional issues may be to blame for the lack of Pt-Fe in the run products. An attempt at method 2 was also made for MnO-Mn_3O_4 buffered runs (logfO_2= -4.10), with the main reason of these experiment being to determine As content while maintaining arsenide saturation. Since no loss of As was noticed with time for these experiments, suggesting no

reaction with the buffer, the removal of the buffer was just a test of the reproducibility of method 2. The As content for M2-SP6 was found to be 14,376.92 ± 804.45 ppm or ~1.4wt%, which is nearly the same as the runs completed with the buffer (e.g. SP7- 14684.32 ± 1681.41 ppm As), which suggests that the run may very well have been saturated in Pt-As, just not visibly in the polished mount.

4.3.1.1 Partitioning of V from Spinel to Melt as a Function of fO_2

According to the work done by Mallmann and O'Neill (2009), the partitioning of vanadium (V) from Cr-spinel to silicate melt may be considered as function of fO_2. This phenomenon acted as a resource for determining the fO_2 of the un-buffered run-products in this study. The theory was applied to two groups of experiments: M2-Sp3/M2Sp4 and M2-Sp5/M2-Sp6, which were equilibrated at a $\log fO_{2\ of}$ -7.72 and -4.10 respectively. Equation 15 (see Mallmann and O'Neill, 2009) provides a function that describes the fO_2 dependence of bulk V partition coefficient, in this case between spinel and silicate melt ($D_v^{sp/m}$), over a range of V oxidation states (e.g.3^+, 4^+, 5^+). By substituting the appropriate fO_2 values used in this study, a reference curve was made to compare results found from the run products (Table 5a). Once the V content of the glass and spinel were determined by means of LA-ICPMS, the resulting $D_v^{sp/m}$ was plotted against the respective fO_2 for each experiment and compared to the curve produced by Mallmann and O'Neill (Figure 14). For a summary of the V content of the spinel and melt along with the oxide composition of the spinel see table 5b.The melt composition used by Mallmann and O'Neill is referred to as Cr-spinel (mix V7) comprised of a variable mix of glass, clinopyroxene, olivine and trace alloy. The difference in melt composition explains the vertical shift in the curve produced from this study; however, much like the reference curve, there is an apparent increase in partitioning of V with decreasing fO_2.

That being said, there is a clear similarity in the $D_v^{sp/m}$ values for both the runs with and without the buffer at each fO_2, implying that the melt remained equilibrated at the buffered fO_2 following the re-melt with the buffer removed. The variations in the spinel and melt V contents bewtween run products (e.g. M2-Sp5 and M2-Sp6) is an issue of total mass exchange, since the experiments were different in size resulting in inconsistent transaction of V species between spinel and melt. The experiments,

however, do plot within two distinct partitioning regimes, with $D_V^{sp/m}$ values of 1.27 and 2.89 at a $logfO_2$= -4.10, and 13.64 and 16.16 at a $logfO_2$= -7.72, which suggest the fO_2 was consistent between the run product groups with and without the buffer.

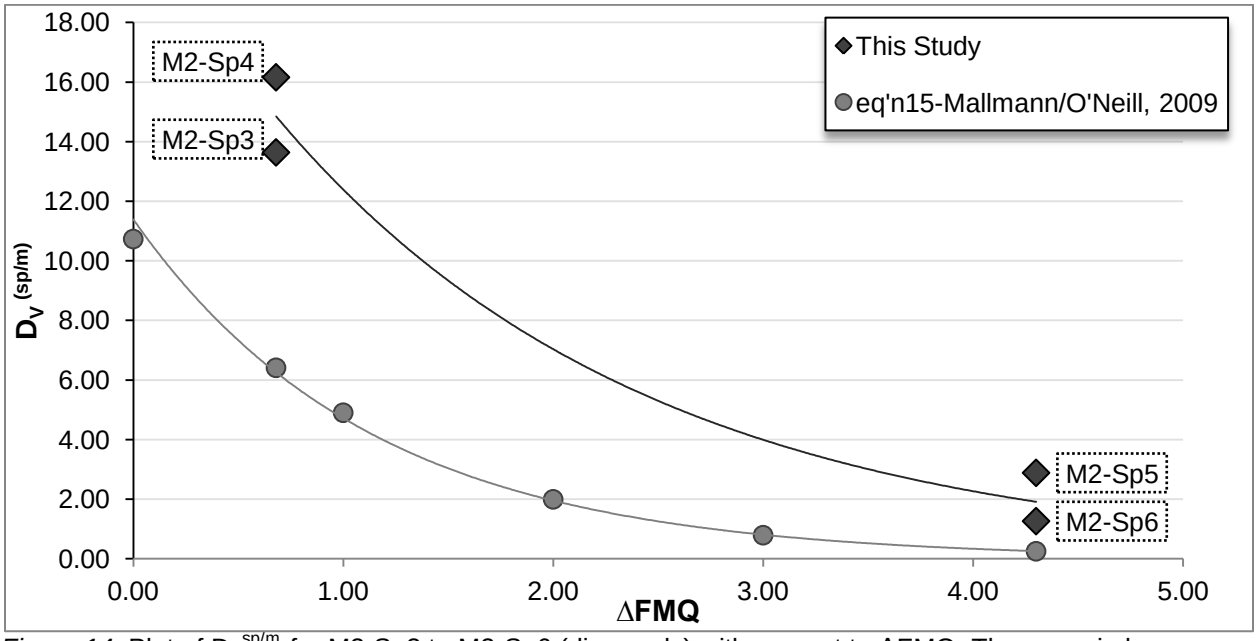

Figure 14: Plot of $D_V^{sp/m}$ for M2-Sp3 to M2-Sp6 (diamonds) with respect to ΔFMQ. The grey circles represent values plotted using equation 15 from Mallmann and O'Neill, 2009. A clear increase in V partitioning from spinel to melt with decreasing fO_2; the run products from method two plot in two distinct regions.

D_{V3+}	D_{V4+}	D_{V5+}	$(K^l_{hom(6a)})^{-1}$	$(K^l_{hom(6b)})^{-1}$	$(K^l_{hom(6c)})^{-1}$	$logfO_2$	fO_2	$D_V^{sp/m}$	ΔFMQ
3.9E+01	3.9	3.0E-03	2.5E-09	3.0E-05	3.1E-03	-8.4	4.0E-09	10.7	0.0
3.9E+01	3.9	3.0E-03	2.5E-09	3.0E-05	3.1E-03	-7.7	1.9E-08	6.4	0.7
3.9E+01	3.9	3.0E-03	2.5E-09	3.0E-05	3.1E-03	-7.4	4.0E-08	4.9	1.0
3.9E+01	3.9	3.0E-03	2.5E-09	3.0E-05	3.1E-03	-6.4	4.0E-07	2.0	2.0
3.9E+01	3.9	3.0E-03	2.5E-09	3.0E-05	3.1E-03	-5.4	4.0E-06	0.8	3.0
3.9E+01	3.9	3.0E-03	2.5E-09	3.0E-05	3.1E-03	-4.1	7.9E-05	0.3	4.3

Table 5a: $D_V^{sp/m}$ values calculated from equation 15 (Mallmann and O'Neill, 2009).Constants were taken from table 6 from the same paper.

		M2-SP3	1σ	M2-SP4	1σ	M2-SP5	1σ	M2-SP6	1σ
	V_{spinel} (ppm)	475.53		563.75		998.08		256.03	
	V_{melt} (ppm)	34.86		34.88		345.70		202.21	
	$D_V^{sp/m}$	13.64		16.16		2.89		1.27	
	ΔFMQ	0.68		0.68		4.30		4.30	
Spinel (wt%)	SiO2	0.12	0.05	0.03	0.01	0.06	0.05	0.11	0.10
	TiO2	0.58	0.16	0.87	0.49	2.93	0.12	4.61	0.49
	V2O3	0.09	0.02	0.09	0.02	0.03	0.01	0.17	0.02
	Al2O3	17.22	1.23	17.77	0.91	11.52	0.23	20.74	1.41
	Cr2O3	46.26	1.43	46.02	1.41	27.09	0.86	30.13	1.73
	FeO	15.70		16.94		17.40		19.39	
	Fe2O3	5.57		3.34		25.79		9.53	
	MnO	0.21	0.01	0.20	0.02	0.22	0.02	0.19	0.01
	MgO	12.01	0.31	11.32	0.58	10.95	0.12	12.20	0.55
	NiO	0.25	0.02	0.03	0.01	0.69	0.03	0.12	0.01
	Total	98.01	0.60	96.61	1.29	96.67	0.52	97.18	1.87

Table 5b: Summary of V content of spinel and melt determined by LA-ICPMS, and oxide composition of spinels from the respective run-products detrermined by EPMA.

4.4 Determination of Pt Solubility as a Function of fO_2

It is assumed that Pt dissolves in silicate melts as an oxide under oxidizing conditions; taking the valence state of Pt ($^{x+}$) into account, this may be expressed as:

$$Pt^{x+}_{(met)} + \frac{x}{4} O_{2(g)} = PtO_{\frac{x}{2}(sil)} \qquad (2)$$

where the subscripts *(met)*, *(g)*, and *(sil)* represent components in metal, gas and silicate phase respectively.

The equilibrium constant for equation 1 (K_{e1}) may be represented as:

$$K_{e_1} = \frac{\left(\left[PtO_{\frac{x}{2}}^{sil}\right]\right)}{\left(\left[Pt^{met}\right] \cdot (fO_2)^{\frac{x}{4}}\right)} \qquad (3)$$

where square brackets denote activities; the over scripts (sil and met) imply the respective phase in which the component is present; and oxygen fugacity is represented by fO_2.

An expression for $\log K_{e1}$ is then:

$$\log K_{e_1} = \log\left[PtO_{\frac{x}{2}}^{sil}\right] - \log\left[Pt^{met}\right] - \frac{x}{4}\cdot\log(fO_2) \qquad (3a)$$

Equation 2a may be rearranged when the system is saturated in Pt metal, where the product of the mole fraction and activity coefficient of species *i* is equal to activity of species *i* (e.g. [*i*] = $X_i \cdot \gamma_i$), yielding the expression:

$$\log X_{PtO_{\frac{x}{2}}}^{sil} = \frac{x}{4}\cdot\log(fO_2) + A \qquad (4)$$

where *A* represents a constant. Assuming Pt concentrations dissolved in the melt are very low at saturation in Pt metal, implying Henry's Law applies, equation 3 shows that solubility of Pt should increase with respect to increasing oxygen fugacity, proportional to $\frac{x}{4}\cdot\log(fO_2)$.The common oxidation state of Pt under oxidizing conditions is 2+, as determined by Borisov and Palme (1997), at a $\log fO_2$ range of 0 to -5 at ~1400°C. However, the development of metal inclusions as micro particles at reducing conditions results in excessive scatter yielded from analytical techniques. The inability to make precise measurements at reducing conditions may be due to a potential change in oxidation state of PGEs at low fO_2.

4.4.1 Corrections for Pt Activity: Effect of Fe in Pt

Since an Fe-bearing melt was used throughout experimentation (~10wt% FeO), the formation of an immiscible Fe-Pt alloy was unavoidable. This characteristic reflects the siderophile tendency for Pt when in the presence of Fe in magmatic systems, which is shared by all other PGEs. In order to properly quantify Pt solubility in the run-products, the Fe portion of the alloys were taken into account.

The relationships derived by Borisov and Palme (2000) provided the definitions to correct for an activity of Pt equal to 1 (*[Pt]=1*) in the melt using the following expressions:

$$\log \gamma_{Pt} = (X_{Fe})^2 \cdot (B + C \cdot (4 \cdot X_{Fe} - 3)) \quad (5)$$

$$\left[Pt\right]^2 = (X_{Pt})^2 \cdot (\gamma_{Pt})^2 \quad (6)$$

$$\left[Pt_{final}\right] = \frac{[Pt_o]}{[Pt]} \quad (7)$$

where γ_{Pt} is the activity coefficient of Pt in the silicate; X_{Fe} and X_{Pt} are the mole fractions of Fe and Pt respectively; the two constants B = –3.326564, and C = 0.221051 are from Heald (1967) and are considered valid estimates over the temperature range of 1130-1550°C. The final activity of Pt ($[Pt_{final}]$) is represented by the initial activity as reported from data reduction ($[Pt_o]$) over the activity found in equation 5 (*[Pt]*). A regular increase in Pt activities was noticed when corrected for activity equal to 1.

4.5 Solubility of Pt in As-Bearing and As-Free Experiments

After investigating the measured Pt solubilities for both As-bearing and As-free experiments, there was a noticeable contrast between the respective quantities for each (See figure 15 and Table 2/Table 4). As a side note, plotting of the solubilities determined from the reducing conditions was done just to display the scatter associated with these values, and no viable results were inferred. On the other hand, there is a distinct difference between Pt concentrations in the Ni-NiO runs, which implies potential for As complexing. The average Pt solubility for the As-bearing Ni-NiO runs was found to be 0.133±0.011 ppm Pt determined from the 24 hr to 70 hr run durations, since the 87 hr run is far too depleted in As due to reaction with buffer to be a representative quantity. In contrast to the measurements of the As-free experiment, a Pt solubility of 0.021±0.009 ppm was found, which indicates that at the same fO_2 the complexing of Pt with only O results in a lower solubility than if an As

component is present. A similar trend was noticed in the MnO-Mn_3O_4 buffered runs, but to a lesser extent. The solubility of the As-bearing experiments was on average 0.191±0.020 ppm Pt; where the As-free experiment resulted in dissolution of 0.141±-0.030 ppm Pt. As mentioned above, all of the MnO-Mn_3O_4 buffered runs were not saturated in the arsenide melt, implying that there is the potential for more As to be dissolved in the melt, which may yield higher Pt solubility if a direct dependence of Pt solubility is assumed to be related to the presence of As. In any case, the variations in the Pt content of the product glasses bearing arsenic, and those not, indicate the possibility of an As component in the melt behaving as a complexing ligand; in turn influencing Pt solubility.

5. Discussion

5.1 Estimation of Arsenic Speciation as a Function of fO_2

Due to the lack of the arsenide melt phase in many of the run-product alloys produced under oxidizing conditions, it is difficult to constrain the average activity of As in the alloys; however, the bulk of the analyses on the runs at ΔFMQ of +0.68 yielded a stable As content at ~15at%, whereas the one analysis of the alloy formed at ΔFMQ of -3.3 was found to contain 22.50at% As (See table 6).

							Arsenide melt at%		
Expt. ID	**T(°C)**	**Buffer**	**log fO_2**	**ΔFMQ**	**Duration (hrs)**	**Glass comp**	**Fe**	**Pt**	**As**
Sp1	1200	Ni-NiO	-7.72	0.68	69.50	C	nd	nd	nd
Sp2	1200	Mo-MoO2	-11.65	-3.25	65	C	nd	nd	nd
Sp4	1202	Mo-MoO2	-11.65	-3.25	87.33	C	4.60	71.90	22.50
Sp5	1202	Ni-NiO	-7.72	0.68	87.33	C	0.02	83.90	14.76
Sp7	1202	MnO-Mn3O4	-4.10	4.30	87.33	C	nd	nd	nd
Sp8	1203	Ni-NiO	-7.72	0.68	23.50	C	0.04	84.40	14.95
Sp9	1203	Ni-NiO	-7.72	0.68	47.66	C	0.03	83.37	15.73
[1]Sp10	1203	Ni-NiO/Mo-MoO2	-11.65	-3.25	178.33	C	nd	nd	nd
Sp14	1202	MnO-Mn3O4	-4.10	4.30	48	C	nd	nd	nd
Sp15	1202	Mo-MoO2	-11.65	-3.25	45.50	C	nd	nd	nd

Table 6: Arsenide melt compositions as determined using EMPA. Note that nd= not determined, and [1]= a two-step equilibration initially at Ni-NiO and then at Mo-MoO_2.

This variation implies that As activity does change with respect to fO_2, but until further analysis of the arsenide alloy of run products at ΔFMQ= 4.30 no decisive conclusion may be made. Despite the minor variation in the activity of As in the alloys, the arsenic content of the silicate melt varies considerably with fO_2, with values of 8-17 ppm at ΔFMQ of -3.3, to as high as ~1-1.5 wt% at ΔFMQ of +4.3, with intermediate solubility of 240-440 ppm at ΔFMQ of +0.68. The changes in As solubility with fO_2 may be expressed by the following dissolution reaction:

$$As_{(PtAs)} + n/4O_{2(g)} = AsO_{n/2(sil)} \quad (8)$$

where (*PtAs*) represents the As dissolved in the metallic PtAs melt, and (*sil*) implies $AsO_{n/2}$ in the silicate melt. Since As exists in nature over a range of valence states (-3 to +5) it is important to comprehend the common oxidation states in which it exists in silicate melts in order to properly model the solubility as a function of fO_2. There is no direct research regarding speciation of As in basaltic composition melts, however, the work completed by Chen and Jahanshahi (2010) on FeO_x-CaO-SiO_2 slags may be used as one of the few analogues suggested. Their measurements of the distribution of As at 1300°C over a given fO_2 range for both calcium ferrite and silicate slags indicate that As exists mainly in a +3 oxidation state, or an As_2O_3 ($AsO_{1.5}$) species. Further investigation by Yoshida et al (2010) into the effect of silicate melt composition on redox behaviour of As using differential pulse voltammetry on a soda-lime-silicate glass suggests that $[As^{3+}]/[As^{5+}]$ ratios and $[As^0]/[As^{3+}]$ may be determined based on melt basicity and the stability of a complex containing As. With the incorporation of alkaline earth metals into the structure of the silicate glasses at different temperatures, they were able to deduce changes to the aforementioned As oxidation state ratios through replacements that take place within the glasses following addition. Around the same time Borisova et al (2010) took interest in the oxidation state of As in peraluminous melts (e.g. macusanite) using an array of analytical techniques, including X-ray absorption spectroscopy (XANES), which resulted in the identification of As^{3+} and As^{5+}. Since the past research bares a slight resemblance in some cases to the experiments completed in this study, it reasonable to assume that As may exist mainly in a 0, 3+, and 5+ state within

the resulting glasses. Although, a vital issue proposed by Chunlin (2010), which pertains to one's experiments, is the suggestion that $\gamma AsO_{1.5}$ (activity coefficient of $AsO_{1.5}$) in the slags may change with fO_2 given that the Fe^{3+}/Fe^{2+} ratio is not constant . Applying this concept to the run-products from this study suggests that over the fO_2 range the Fe^{3+}/Fe^{2+} ratio is varying in each resulting glass, and as noted Yoshida et al (2010), since As speciation may in fact be affected by changes in melt basicity, then quantifying the species based strictly on fO_2 may does not account for these inherent variations. For the purpose of modeling, however, it is assumed that the variations in melt basicity is negligible, and all other components remain constant resulting in a purely fO_2 dependent As speciation. In this case, the total As content may then be modeled by summing the contributions of As^0, As^{3+}, As^{5+} species, and their respective concentrations, for each $[AsO_{n/2}]$ species, which may be represented by the solubility product:

$$Q^{n+} = \left[AsO_{n/2}\right] / fO_2{}^{n/4} \qquad (9)$$

Which, summing over all species present yields the relation:

$$As_{total} = \sum Q^{n+} \cdot fO_2{}^{n/4} \qquad (10)$$

Informed by previous work on arsenic speciation, the arsenic solubility as a function of fO_2 measured in this study is modeled by iteratively changing values of Q^{n+} until a best fit is obtained for the data. Note that for the neutral As species, the model value for Q^0 is the limiting solubility at low fO_2. The model curve produced in Figure 15 was found to be the closest fit to the solubilities measured from the run-products, where only Q^0 and Q^{3+} were considered to significantly contribute to the model (See table 7 for accompanying data). If this assumption is correct, then As^0 and $As^{2+}$are the predominant oxidation states in the glasses over the given fO_2 range.

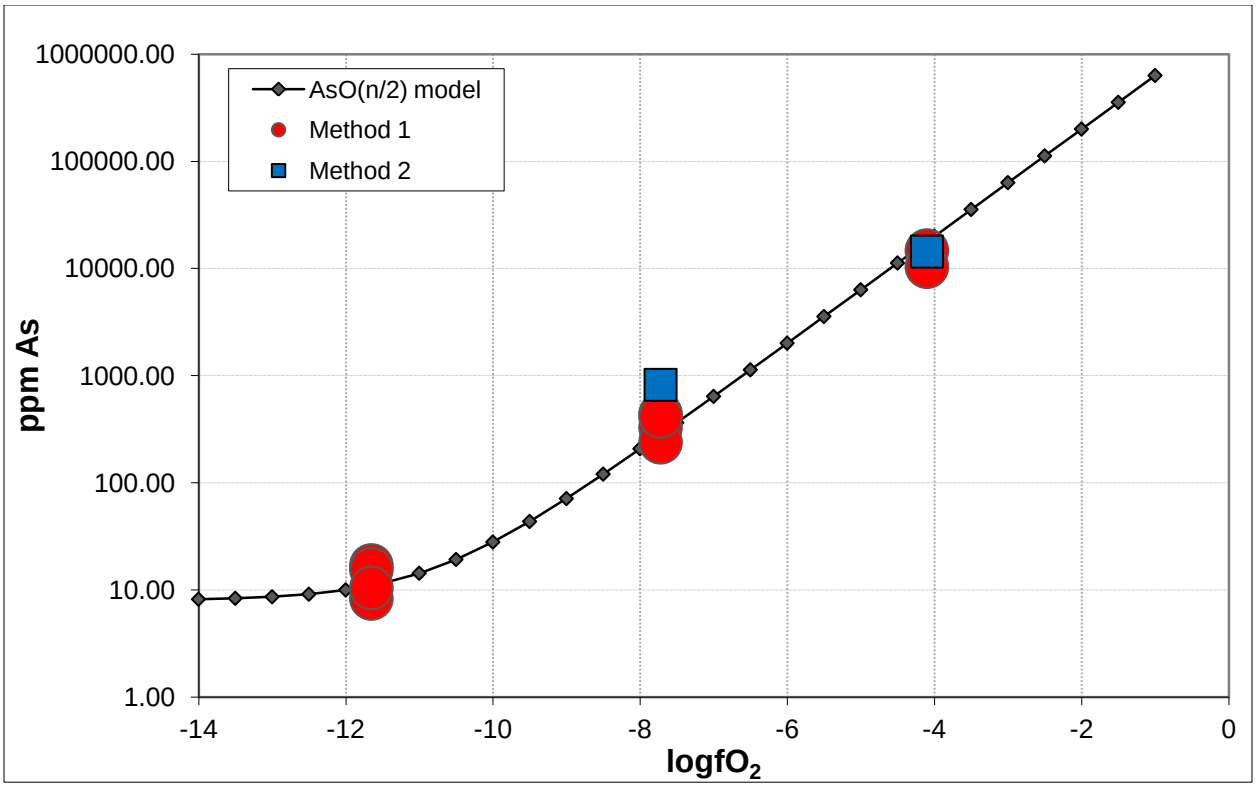

Figure 15: Attempt at modeling arsenic speciation in the run-product glasses, using equation *(10)*. See table 2 for the solubilities measured in the As-bearing experiments, and table 5 for the parameters and the resulting quantities determined for the model curve.

$logfO_2$	fO_2	$fO_2^{0.5}$	$fO_2^{0.75}$	$fO_2^{1.25}$	Model As (ppm)
-1	1.00E-01	3.16E-01	1.78E-01	5.62E-02	632463.53
-2	1.00E-02	1.00E-01	3.16E-02	3.16E-03	200008.00
-3	1.00E-03	3.16E-02	5.62E-03	1.78E-04	63253.55
-4	1.00E-04	1.00E-02	1.00E-03	1.00E-05	200008.00
-5	1.00E-05	3.16E-03	1.78E-04	5.62E-07	6332.56
-6	1.00E-06	1.00E-03	3.16E-05	3.16E-08	2008.00
-7	1.00E-07	3.16E-04	5.62E-06	1.78E-09	640.46
-8	1.00E-08	1.00E-04	1.00E-06	1.00E-10	208.00
-9	1.00E-09	3.16E-05	1.78E-07	5.62E-12	71.25
-10	1.00E-10	1.00E-05	3.16E-08	3.16E-13	28.00
-11	1.00E-11	3.16E-06	5.62E-09	1.78E-14	14.32
-12	1.00E-12	1.00E-06	1.00E-09	1.00E-15	10.00
-13	1.00E-13	3.16E-07	1.78E-10	5.62E-17	8.63
-14	1.00E-14	1.00E-07	3.16E-11	3.16E-18	8.2

Table 7: Determined quantities for the model curve in Figure 15 using equation *(10)*. The values for Q^{n+} were set as follows: Q^0=8, Q^{2+}= 2.00E6, Q^{3+}=0and Q^{5+}= 0. Note that a finer $logfO_2$ scale was used in Figure 15 (in increments of 0.5 $logfO_2$ units). Refer to table 2 and table 4 for the measured solubilities at each fO_2.

5.2 Modeling Pt-O and Pt-As Complexing in Silicate Melts

The variation in Pt solubility in the melt may arise through interactions with both oxygen and arsenic. Obviously those experiments containing no As are considered to be strictly complexing with O, forming a PtO species dissolved in the silicate melt (equation *2*). Whereas, the experiments bearing As may be dissolving Pt as result of Pt-O, Pt-As or Pt-As-O interactions. First off, the attempt at modelling the PtO component was completed using the same method noted earlier for determining As speciation as a function of fO_2, since Pt speciation also has a distinct dependence on fO_2. For the purpose of displaying solubilities over a larger fO_2 range, Dr. James Brenan at the University of Toronto provided supplemental data for experiments depicting Pt solubility in the same melt composition at the same temperature over a wider fO_2 range (see Figure 16). By substituting a $PtO_{n/2}$ species into equation *(10)* according to the dissolution reaction noted in equation *(2)*, the resulting expression for total Pt (Pt_{total}) in the melt may be represented as:

$$Pt_{total} = \sum Q^{n+} \cdot fO_2{}^{n/4} \qquad (11)$$

By once again adjusting the values for Q^{n+} for each Pt oxidation state, one was able to fit a suitable curve to the measured solubilities. Note that the Q^0 species determined the solubility at low fO_2. The resulting curve as seen in Figure 16 is assumed to be the best fit according to the measured solubilities at each fO_2, when considering only Pt-O complexing.

Due to the inability to determine As fugacity (fAs_2) in the experiments, it is not reasonable to model the Pt-As or Pt-As-O complexing strictly as a function of fO_2. For this reason, a hypothetical ideal curve was fit to the data, and it is suggested that the line is constrained by the main reaction:

$$Pt_{(met)} + \frac{1}{2} As_{2(g)} = PtAs_{(sil)} \quad (12)$$

However, since O may actually be complexing with Pt simultaneously with As, a Pt-As-O interaction is a more likely dissolution mechanism. Due to the prior modeling of As speciation in the melt revealing As^{2+} as a major constituent, it may be possible for Pt^{x+} to be reacting with an AsO_3^{3-} ligand in a gaseous phase to produce $Pt(AsO_3)_x$ species dissolved in the melt; which may be expressed as:

$$Pt^{x+}_{(met)} + AsO_3{}^{3-}_{(g)} = Pt_3(AsO_3)_{x(sil)} \quad (13)$$

It is important to note that until further research is completed this stands as a hypothetical relationship and is strictly presented as a thought experiment.

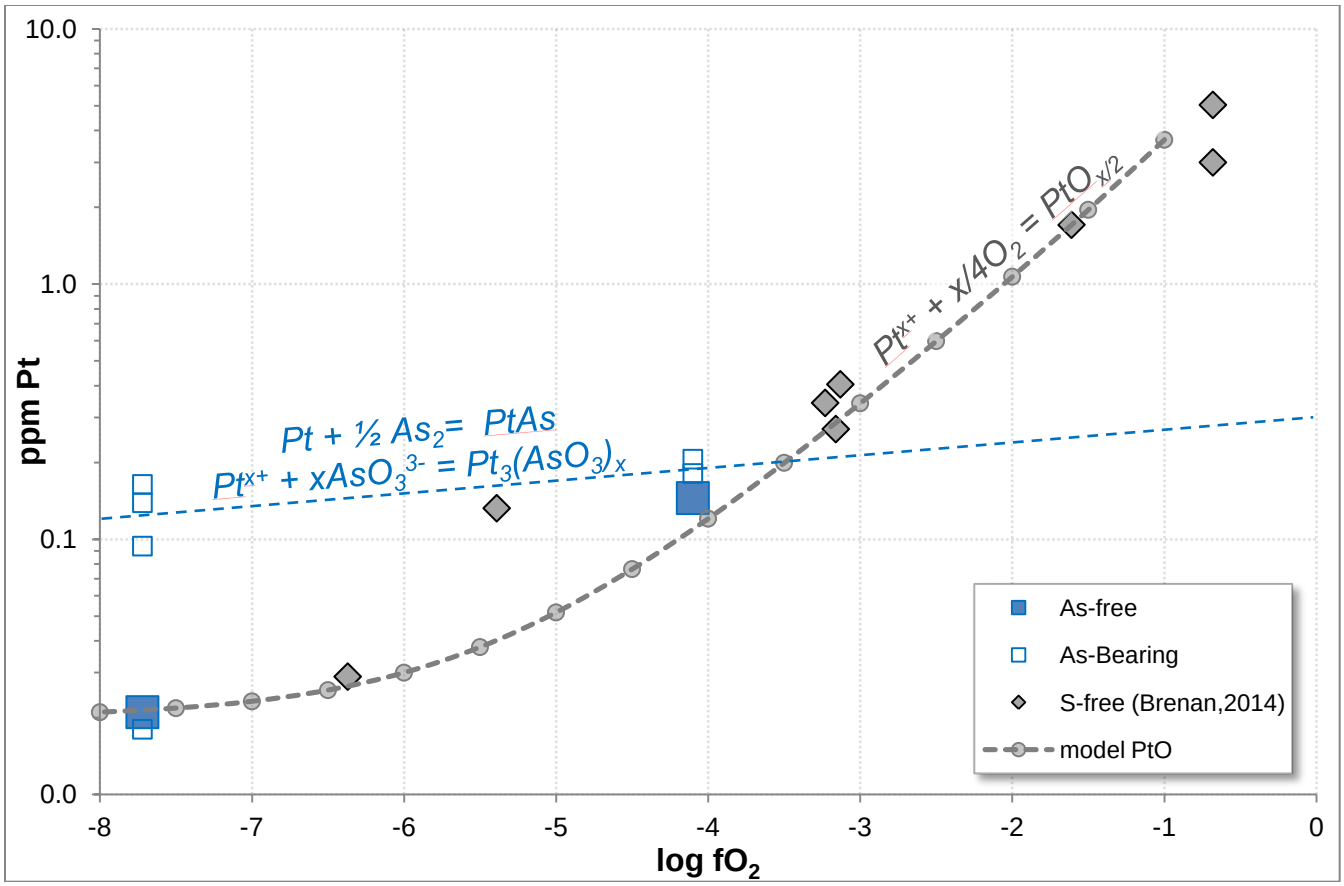

Figure 16: Summary plot of Pt solubility, including experiments completed by Brenan (2014). The reaction stated above each model curve represents the reaction controlling the dissolution of Pt in the silicate melt. Note that the Blue dashed line indicates a hypothetical ideal curve fit to represent both As and As-O complexing with Pt in the melt. According the line fit to the As-bearing solubilities it is apparent at a logfO_2>-4, equation *(2)* is the controlling reaction and Pt is dissolved mainly as an oxide. However, when logfO_2<-4 there is an indication of Pt-As and Pt-As-O complexing according to equations *(12)* and *(13).* See table 8 for model solubilities.

logfO_2	fO_2	$fO_2^{0.5}$	$fO_2^{0.75}$	Model [Pt]
-1	1.00E-01	3.16E-01	1.78E-01	3.682
-2	1.00E-02	1.00E-01	3.16E-02	1.070
-3	1.00E-03	3.16E-02	5.62E-03	0.341
-4	1.00E-04	1.00E-02	1.00E-03	0.121
-5	1.00E-05	3.16E-03	1.78E-04	0.052
-6	1.00E-06	1.00E-03	3.16E-05	0.030
-7	1.00E-07	3.16E-04	5.62E-06	0.023
-8	1.00E-08	1.00E-04	1.00E-06	0.021

Table 8: Accompanying data for the modeling of PtO complexing in the silicate melt as a function of fO_2. The respective values for Q^{n+} were assumed to be: Q^0= 0.02, Q^{2+}=5.00, Q^{3+}= 10.00, and Q^{4+}=0. Note this is determined from As and S free solubilities, so only O is considered as the complexing ligand.

5.3 Effect of Natural As Levels on Pt Solubility

The abundant analyses of basalts from several different localities compiled by Jenner and O'Neill (2012) serve an excellent source for determining natural As content in primitive basalts. In order to determine the appropriate As concentration in relationship to one's melt composition, the MgO wt% as determined by EPMA was plotted against the respective ^{75}As content reported from LA-ICPMS analyses for each sample (Figure 17). Since primitive basalts are considered to contain greater than 8 wt% Mgo, the average As concentrations for all those samples above this content were considered a representative measurement of natural levels of As. After calculating the average As concentration for the suitable samples, it was found that ~0.125ppm As is the natural concentration for a primitive basalt. Since the run-products in this study at ~FMQ+1 (Ni-NiO buffer), which is near the approximate fO_2 for a primitive basalt, yielded ~400ppm As it is clear that the affect of As would be much less at natural levels. Assuming a one to one relationship between As content and Pt solubility, the Pt dissolution as result of As complexing in a primitive basalt at 0.125ppm As would be 4.16E-5 ppm (See figure 18). This implies that unless there is direct contact with an As source (e.g. arsenide melt), As complexing is not a significant complexing ligand in a primitive basalt.

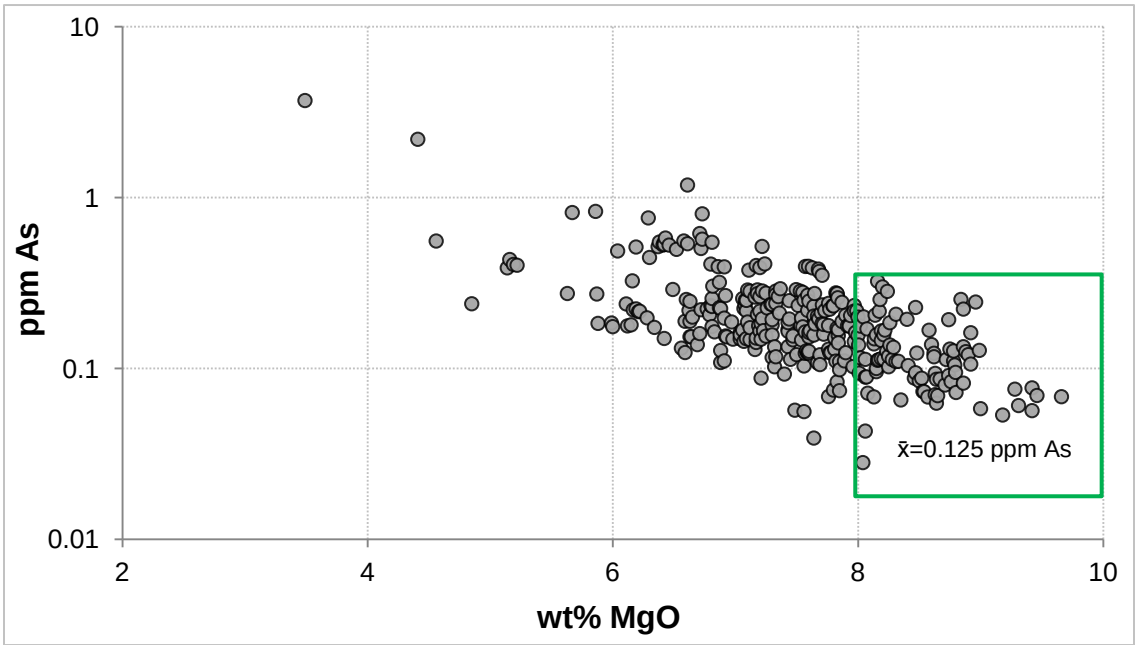

Figure 17: Plot of analyses completed by Jenner and O'Neill (2012). The green box indicates the area used to determine an average As content of 0.125ppm for a primitive basalt.

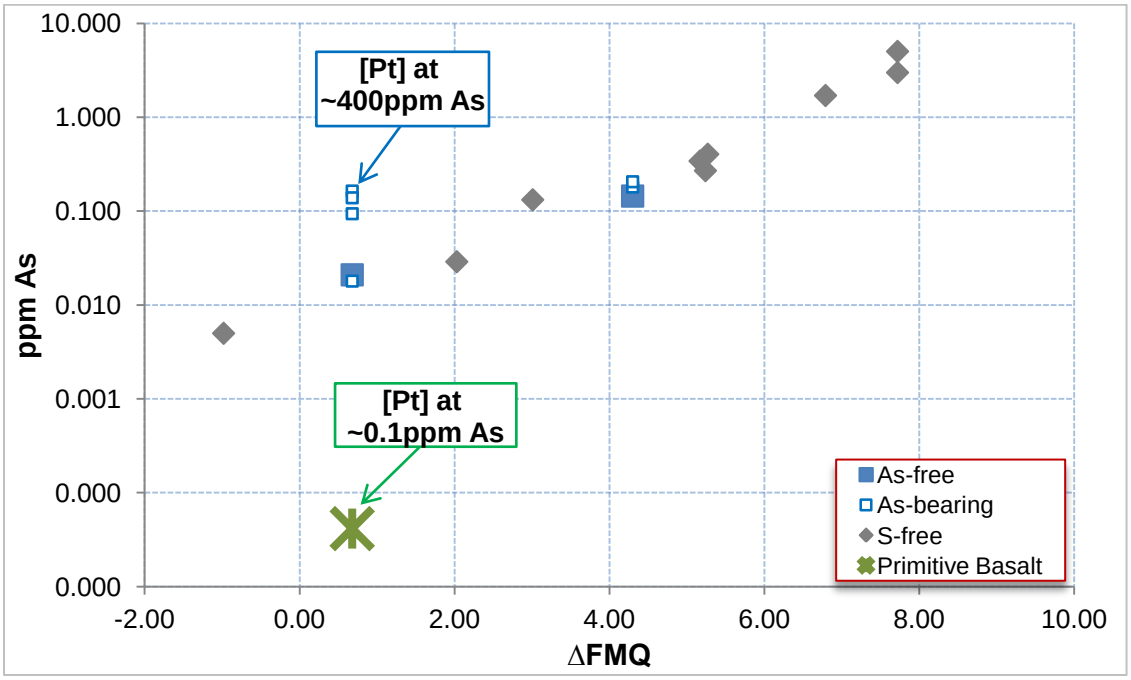

Figure 18: Relative Pt solubility for a primitive basalt (4.16E-5ppm Pt- green star) in comparison to those measured in the Ni-NiO runs (0.133ppm Pt-open blue square) at ΔFMQ=0.68. It is clear that As plays a minor role in enhancing solubility of Pt at natural levels.

6. Conclusion

After review of the results yielded from the suite of experiments, it is clear the Pt solubility is affected when in the presence of As at a specific fO_2 range. In some cases (e.g. at the Ni-NiO buffer) complexing with As seems to enhance the solubility of Pt to even greater concentrations than when complexing with O alone. The solubility of Pt in these experiments was increased from 0.010ppm Pt in the As-free experiment to as high as 0.165ppm Pt at the shortest run duration when As was present. The attempt at modeling Pt solubility reveals that in As-free experiments a strictly Pt-O interaction is at hand as explained by equation *(2)*, and those containing As dissolve Pt into the melt by way of reaction *(12)* and *(13)* through simultaneous interaction between Pt, As, and O. Also, the proper precautions must be taken in order to remove metallic contamination in the glasses at reducing conditions, such that constraints may be imposed on Pt solubilities. Significance of the mechanisms for As complexing in natural primitive basalts is low, due to the much lower natural As levels relative to the amount dissolved

in the glasses of this study (natural basalt= ~0.1ppm As, SP8=437.9±48.1 ppm As). There are, however, reasons to believe that the As speciation as determined from this study may be applicable to conditions similar to those in nature- such as if a large As source were to contact a silicate melt during formation. The dramatic change in As solubility from 8-17 ppm at ΔFMQ= -3.3 to ~1-1.5 wt% at ΔFMQ= +4.3, suggests that there is a direct dependence of As solubility on fO_2, and the main oxidations states of As in these experiments is As^0 and As^{2+}. Based on the results of these experiments, it is clear that relationship between As in igneous systems and Pt solubility is a multifaceted and still misunderstood area of research. Hopefully this study acts as a basis for future investigations, and sparks the interest of others to examine this exciting area of geochemistry.

7. References Cited

Bennett, N. R., & Brenan, J. M. (2013). Controls on the solubility of rhenium in silicate melt: Implications for the osmium isotopic composition of Earth's mantle. *Earth and Planetary Science Letters*, *361*, 320-332.

Borisov, A., & Palme, H. (1995). The solubility of iridium in silicate melts: New data from experiments with Ir< sub> 10</sub> Pt< sub> 90</sub> alloys.*Geochimica et Cosmochimica Acta*, *59*(3), 481-485.

Borisov, A., & Palme, H. (1997). Experimental determination of the solubility of platinum in silicate melts. *Geochimica et Cosmochimica Acta*, *61*(20), 4349-4357.

Borisov, A., & Palme, H. (2000). Solubilities of noble metals in Fe-containing silicate melts as derived from experiments in Fe-free systems. *American Mineralogist*, *85*(11-12), 1665-1673.

Borisov, A., Palme, H., & Spettel, B. (1994). Solubility of palladium in silicate melts: implications for core formation in the Earth. *Geochimica et Cosmochimica Acta*, *58*(2), 705-716.

Borisova, A. Y., Pokrovski, G. S., Pichavant, M. I. C. H. E. L., Freydier, R. É. M. I., & Candaudap, F. (2010). Arsenic enrichment in hydrous peraluminous melts: Insights from femtosecond laser ablation-inductively coupled plasma-quadrupole mass spectrometry, and in situ X-ray absorption fine structure spectroscopy. *American Mineralogist*, *95*(7), 1095-1104.

Capobianco, C. J., Jones, J. H., & Drake, M. J. (1993). Metal-silicate thermochemistry at high temperature: Magma oceans and the “excess siderophile element” problem of the Earth's upper mantle. *Journal of Geophysical Research: Planets (1991–2012)*, *98*(E3), 5433-5443.

Chen, C., & Jahanshahi, S. (2010). Thermodynamics of Arsenic in FeOx-CaO-SiO2 Slags. *Metallurgical and Materials Transactions B*, *41*(6), 1166-1174.

Ertel, W., O’Neill, H. S. C., Sylvester, P. J., & Dingwell, D. B. (1999). Solubilities of Pt and Rh in a haplobasaltic silicate melt at 1300 C. *Geochimica et Cosmochimica Acta*, *63*(16), 2439-2449.

Fonseca R. O. C., Campbell I. H., O'Neill H. St. C. and Allen C. (2009) Solubility of Pt in sulphide mattes: Implications for the genesis of PGE-rich horizons in layered intrusions. Geochimica et Cosmochimica Acta 73, 5764-5777.

Hanley, J. J. (2007). The role of arsenic-rich melts and mineral phases in the development of high-grade Pt-Pd mineralization within komatiite-associated magmatic Ni-Cu sulfide horizons at Dundonald Beach South, Abitibi Subprovince, Ontario, Canada. *Economic Geology*, *102*(2), 305-317.

Heald, E.F. (1967) Thermodynamics of iron-platinum alloys. *Transactions of Metallurgical Society* AIME, 239, 1337–1340.

Jenner, F. E., & O'Neill, H. S. C. (2012). Analysis of 60 elements in 616 ocean floor basaltic glasses. *Geochemistry, Geophysics, Geosystems*, *13*(2).

Laurenz, V. (2012). *Effect of iron and sulfur on the solubility of highly siderophile elements in silicate melts* (Doctoral dissertation, Universitäts-und Landesbibliothek Bonn).

Maier, W. D., & Barnes, S. J. (1999). Platinum-group elements in silicate rocks of the lower, critical and main zones at union section, Western Bushveld Complex. *Journal of Petrology*, *40*(11), 1647-1671.

Mallmann, G., & O'Neill, H. S. C. (2009). The crystal/melt partitioning of V during mantle melting as a function of oxygen fugacity compared with some other elements (Al, P, Ca, Sc, Ti, Cr, Fe, Ga, Y, Zr and Nb). *Journal of Petrology*, *50*(9), 1765-1794.

Mungall, J., & Brenan, J. (2014). Partitioning of platinum-group elements and Au between sulfide liquid and basalt and the origins of mantle-crust fractionation of the chalcophile elements. *Geochimica et Cosmochimica Acta*, *125*, 265-289.

O'Neil, H. S. C. (1986). Mo-MoO_2 (MOM) oxygen buffer and the free energy of formation of MoO_2. *American Mineralogist*, *71*, 1007-1010.

O'Neill, H. S. C., & Pownceby, M. I. (1993). Thermodynamic data from redox reactions at high temperatures. II. The MnO-0Mn3O4 oxygen buffer, and implications for the thermodynamic properties of MnO and Mn3O4.*Contributions to Mineralogy and Petrology*, *114*(3), 315-320.

Piña, R., Gervilla, F., Barnes, S. J., Ortega, L., & Lunar, R. (2013). Partition Coefficients of Platinum Group and Chalcophile Elements Between Arsenide and Sulfide Phases as Determined in the Beni Bousera Cr-Ni Mineralization (North Morocco). *Economic Geology*, *108*(5), 935-951.

Yoshida, S., Sudo, T., Kato, M., Sugawara, T., Matsuoka, J., Miura, Y., & Kii, Y. (2010). Effects of composition on redox behaviors of antimony or arsenic ion in silicate melts by differential pulse voltammetry. *Journal of Non-Crystalline Solids*, *356*(50), 2842-2849.